Robotica (2026), **44**, pp. 630–658
doi:10.1017/S0263574726103257

CAMBRIDGE UNIVERSITY PRESS

RESEARCH ARTICLE

A soft growing robotic system for odor detection and classification‡

Ayodele James Oyejide[1], Ahmet Astar[2], Gülnur Kaya[3], Ustaz Abdulfattah Yaqub[2], Eray A. Baran[4] and Fabio Stroppa[2]

[1]Electrical and Electronics Engineering, Kadir Has University - Kadir Has Campus Cibali, Istanbul, Türkiye
[2]Computer Engineering, Kadir Has University - Kadir Has Campus Cibali, Türkiye
[3]Mechatronics Engineering, Kadir Has University - Kadir Has Campus Cibali, Türkiye
[4]Faculty of Engineering and Natural Sciences, Mechatronics Engineering, Istanbul Bilgi University, Türkiye
Corresponding author: Ayodele James Oyejide; Email: aoyejide@stu.khas.edu.tr

Received: 11 December 2024; **Revised:** 12 December 2025; **Accepted:** 27 January 2026;
First published online: 10 March 2026

Keywords: biologically inspired robots; E-nose; machine learning; soft growing robots; olfactory robotics

Abstract

Odor classification is essential in environmental monitoring, gas leak detection, and industrial safety. Although conventional mobile robotic platforms equipped with electronic noses offer advanced gas-sensing capabilities, their performance in confined or cluttered environments is often constrained by rigid structures and limited maneuverability. In this work, we present an *olfactory softgrowing robot* (oSGR) that integrates bio-inspired, growth-based locomotion with machine-learning (ML)-driven odor classification. Our system comprises a pressurized base enabling contact-free eversion and a custom motorized tip mount housing a multi-sensor array of four metal oxide TGS sensors (2600, 2602, 2611, and 2620) coupled with a passive aspirator for volatile organic compound (VOC) sampling. We provide detailed modeling, design, and structural characterization of the tip mount under multiple actuation configurations, and demonstrate the robot's olfactory capability through experiments involving four VOCs – ethanol, methane, gin, and acetone. We evaluated two experimental modes: (i) in-transit and static sampling at fixed distances (20, 40, and 80 cm from the source), and (ii) continuous sampling during transit at speeds of 5 cm/s and 10 cm/s. The collected olfactory dataset was used to train twelve widely employed supervised ML classifiers in gas sensing, including k-Nearest Neighbors (kNN), Random Forest, and Linear Discriminant Analysis. The kNN classifier achieved the highest accuracy (99.88%), demonstrating strong robustness for the olfactory data. Our results highlight the potential of SGRs for contact-free, continuous, in-motion chemical sensing. This unique data acquisition approach reduces detection latency and energy consumption typically associated with conventional stop-and-sense strategies.

1. Introduction

Inspired by the olfactory system of animals, the technological concept of electronic noses (E-noses) has gained extensive application in odor studies such as odor-source localization [1], plume tracking [2], and gas distribution mapping [3] using robots with sensor arrays [4]. Odor classification in both grounded and mobile robotic systems is a common focus in the field of e-nose applications [5–7]. The grounded systems use a three-phase sampling process: first, exposing the sensor array to a reference gas, then to a target gas for a set period, and finally, analyzing the results based on the steady-state response of the sensors [8]. A similar approach is used on mobile robots, which requires the robots to stop each time an odor sample is to be collected [9]. Applications that require continuous measurement of the environment at different locations, such as pollution monitoring or leak detection, benefit more from mobile robot classification [10, 11].

‡This article has been updated since original publication. A notice detailing the change has been published.

© The Author(s), 2026. Published by Cambridge University Press. This is an Open Access article, distributed under the terms of the Creative Commons Attribution licence (https://creativecommons.org/licenses/by/4.0/), which permits unrestricted re-use, distribution and reproduction, provided the original article is properly cited.

https://doi.org/10.1017/S0263574726103257 Published online by Cambridge University Press

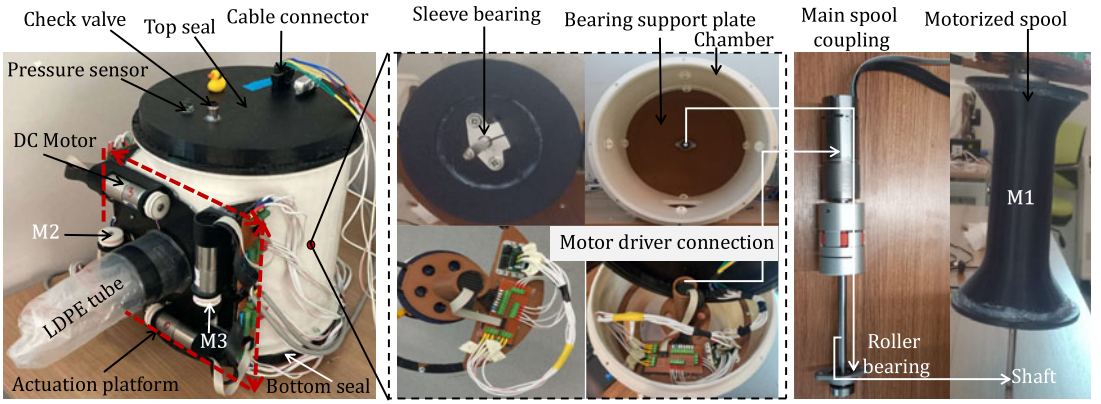


Figure 1. *The developed robot base incorporates a vertically mounted* 20 *cm motorized bioconical spool system (far right). The spool is driven by a Faulhaber brushless DC motor (*11 *cm length), whose shaft interfaces with a* 4 *cm outer-diameter coupling on one end and an* 0.8 *cm D-profile shaft on the other. The shaft is supported by a sleeve bearing, ensuring smooth rotation under low shaft displacement. The spool assembly is enclosed within the base chamber and constrained between two structural plates: an upper mounting plate that supports the motor and provides space for the motor driver, and a lower plate with a roller bearing to minimize rotational resistance (middle block). The chamber is sealed with end caps to prevent air leakage. The complete base structure stands* 34 *cm tall. A frontal platform accommodates four directional actuators (red dashed region), and a mid-height outlet of* 8.5 *cm in outer diameter and* 8 *cm long guides the everted robot body. This geometry positions the inflated body approximately* 15.5 *cm above ground level during eversion.*

However, most odor classification studies with traditional robots are conducted in structured or constrained environments with relatively large workspaces, and mobile robots require several actuators to move and extend their degrees of freedom [12]. Some limitations of the traditional mobile robots have been compensated through extensive design approaches, including navigation through artificial vision and chemical sensing [13–15], swarm intelligence algorithms to improve motion efficiency [16], open sampling systems [7, 17, 18], and localization via adaptive bio-inspired navigation using fuzzy inference methods [19]. Furthermore, in a quest to improve the flexibility and maneuverability of these robots, recent studies have explored bio-inspired soft robots, such as worm-inspired robots for pipe inspection [20–23]. However, these robots suffer from a notable drawback in pipe exploration and even open space, particularly the amount of energy used to propel themselves against the pipe walls, which also generates unwanted vibrations and friction in the system [24].

A more promising alternative to address these challenges is another bio-inspired class of soft robots known as *vine* or soft-growing robots (SGRs) [25]. These robots are air-driven and mimic the growth behavior of vine plants. Constructed from low-density polyethylene (LDPE) or fabric, they are built into inverted tubes and wound on a motorized spool within a pressurized chamber or base station (Figure 1). Growth is achieved by applying compressed air at the inverted tip as the spool unwinds the LDPE material [26]. Due to advancements in modeling [27, 28], task planning [29, 30], tool attachment techniques [31, 32], and actuation/steering techniques [33–35], these robots possess the potential for multi-degrees of freedom and maneuverability. They can grow and retract (i.e., evert) over long distances through passive environments [36] or teleoperated steering [37, 38] while carrying tools such as cameras or sensors [32]. Their performance has also been improved recently through machine-learning (ML) techniques, with work on reinforcement learning for obstacle-aware navigation [39, 40] or other methodologies for sensing and control enhancement [41–43].

In this study, we introduce the concept of *olfactory soft growing robot* (oSGR) for gas detection and classification tasks. As illustrated in Figure 2, the proposed system consists of a pneumatically actuated SGR equipped with a tip-mount device. This tip mount facilitates olfactory sensing by housing an electronic nose (comprising four metal–oxide gas sensors: TGS2600, TGS2602, TGS2611, and TGS2620)

https://doi.org/10.1017/S0263574726103257 Published online by Cambridge University Press

together with a passive aspirator. We present the modeling, design, and characterization of the tip-mount device under various eversion and bending configurations. Additionally, we demonstrate the capabilities of the olfactory SGR through data collection in two scenarios: (i) *in-transit and static sampling*, where data were recorded over 60 seconds at three distances – 20 cm, 40 cm, and 80 cm – following brief motions of 10 s, 20 s, and 40 s, respectively, conducted at a constant approach speed of 2 cm/s; and (ii) *dynamic sampling*, in which the robot continuously advanced toward the odor source along a 100 cm path at speeds of 5 cm/s and 10 cm/s.

The sensor data were subsequently preprocessed and used to train and evaluate twelve different classification models to assess the feasibility of our proposed robot for autonomous odor classification. Our experiments demonstrate successful eversion of the robot with the tip mount and reliable olfactory sensing through the passive aspirator. Additionally, results from the ML classification indicate that the raw olfactory data collected during the robot's motion are inherently separable across different odor classes, even under varying source proximities and approach velocities.

The contributions and scope of this work are as follows:

i. Design and implementation of a pneumatically driven SGR capable of everting through confined environments while lifting a tip-mounted device without physical contact;
ii. Modeling, development, and characterization of a compact, motorized tip-mounted mechanism for transporting multiple sensors on-board without hindering the growth or flexibility of the SGR; and
iii. oSGR enabled the collection of static and dynamic cross-sensitivity olfactory data, integrated into an ML pipeline to establish a foundation for future autonomous gas classification in SGR systems.

The rest of the work is structured as follows: Section 2 provides a background to key concepts; Section 3 presents the robotic system description; Section 4 presents the ML-classification methodology; Section 5 presents demonstrations, experiments, and their results; Section 6 presents ML-based classification with the experimental data; Section 7 discusses the results; and finally Section 8 concludes the work with some future work ideas.

2. Background

This section presents an overview of olfactory robotics, focusing on its concept and recent developments. We also discussed odor classification as a key application within olfactory robotics, emphasizing various algorithms and ML models used in existing research, along with current challenges and progress in the field. The section concludes with a summary of notable applications of SGR systems, and also introduces the concept of oSGR.

2.1. Olfactory robotics

Although often considered pollutants, odors in compounds provide significant benefits for environmental monitoring, particularly in gas leak detection, where the human olfactory system alerts individuals before they are exposed to hazardous levels of harmful substances [44]. However, this detection procedure must not be performed by humans through smell, as it can lead to various health issues, such as dizziness or long-term damage to the olfactory nerves due to toxic exposure [45]. Additionally, in confined environments such as gas lines and scenarios with different volatile organic compounds (VOCs), the human smell is not sufficient. This makes assistive technologies essential to identify and access odor sources. To address this challenge, researchers have turned to biomimicry and bio-inspired engineering – i.e., the development of olfactory tools mimicking the sensing abilities of animals such as dogs and insects [46, 47]. These tools, known as e-noses, function as artificial odor sensors and are typically mounted on stationary structures or mobile robots [48, 49] to collect static and dynamic data, respectively.

https://doi.org/10.1017/S0263574726103257 Published online by Cambridge University Press

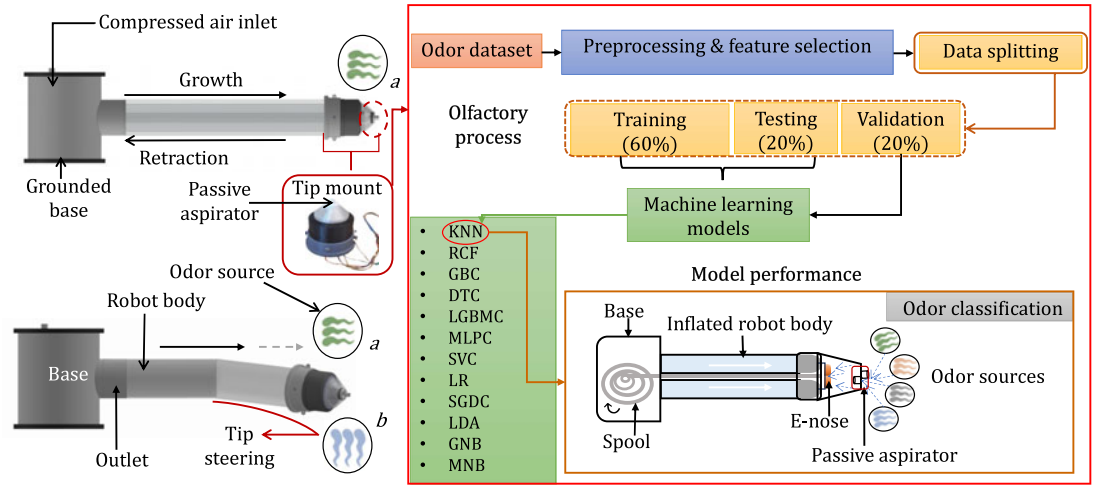


Figure 2. *Conceptual framework. (a) CAD rendering (Left) of the olfactory SGR system demonstrating one-dimension (top) and two-dimensional growth (bottom) toward a target odor source. A full eversion cycle occurs when the robot grows and retracts back to its initial position in the base. The e-noses are transported through a tip-mounted mechanism (see Figure 4 for details). (Right) Olfactory process: The robot uses four e-noses (TGS 2600, 2602, 2611, and 2220) to collect raw data in both static and transit readings. The collected data are then processed into a machine-learning pipeline for autonomous gas classification tasks in SGR systems. We allocated* 60% *of this data for training twelve different ML models,* 20% *for testing, and* 20% *for validation. The test results show that the k-Nearest Neighbors (KNN) classifier outperformed all other models with an accuracy of* 99.88%.

Researchers have explored various applications of static and mobile olfactory robotic systems. For instance, Gonzalez et al. [50] developed the multi-chamber electronic nose to address the long recovery times typically required by metal oxide semiconductor technology after gas exposure. Maho et al. [51] designed an optoelectronic olfactory robotic system for long-term gas discrimination. Harianto et al. [52] implemented an e-nose on an omnidirectional robot, while Abdelkhalek et al. [6] introduced a compact, embedded e-nose for both volatile and non-volatile odor classification in robotics. Xing et al. [53] and Fan et al. [54] demonstrated gas discrimination and mapping capabilities for emergency response scenarios using mobile robots, including the FireNose system, which can navigate harsh environments. A study by Pique et al. [55] explored a smell-driven soft robotic arm for navigation, and Burgues et al. [56] presented a high-bandwidth e-nose for rapid tracking of turbulent plumes. Liu et al. [57] developed a star-nose-inspired tactile-olfactory bionic sensing array for robust object recognition in non-visual environments, and Sanchez et al. [58] introduced a configurable smart e-nose for spatio-temporal olfactory analysis. Collectively, these studies offer design concepts and prototypes that demonstrate how robotic mobility and agility can effectively enhance the transport and deployment of e-noses for both domestic and field applications.

2.2. Odor classification in olfactory robots

Odor classification is the technique of recognizing and classifying various odors according to their chemical makeup and sensory quality [59]. In nature, odors are picked up by specialized receptors reacting to VOCs, enabling humans to discern between different scents [60]. These specialized receptors are mimicked by olfactory sensors and e-noses, which are often deployed by robotic systems, such as the one shown in Figure 2.

To boost odor classification of olfactory robots, either in static or mobile applications, researchers have used several algorithms and ML models. For instance, support vector machine (SVM) has been used to aid the classification of three different VOCs; ethanol, methanol, and acetone, using three TGS

https://doi.org/10.1017/S0263574726103257 Published online by Cambridge University Press

sensors (2,600, 2,602, and 2,620) from a static position, with the robot achieving 95% accuracy [61]. Another study used a metal oxide semiconductor e-nose and a KNN classification algorithm to differentiate between four fruits and juices on a static robot [6]. This study achieved a classification accuracy of 98%. Yan et al. [62] evaluated a fuzzy linguistic odor cognition method for robotic olfaction. This approach centers on realizing a knowledge representation inspired by the brain using fuzzy language rules, which outperforms methods like SVM in uncontrolled, realistic conditions. Furthermore, continuous time recurrent neural networks built on evolutionary robotics were presented by De et al. [15] using a simulated robot with chemical and wind direction e-noses. The approach proves effective for odor-source localization. Li et al. [63], on the other hand, utilized an ensemble learning method found to enhance active perception in robot electronic noses. Additional approaches to odor classification in olfactory robots include deep learning with feature extraction, a hybrid neuromorphic-bayesian model, and localization using vision and fusion navigation algorithms [64–66].

However, in contrast to the static odor detection problem, odor classification in a mobile olfactory system (e-nose installed on a moving platform) introduces open challenges, mostly because existing e-noses show a notable delay in both response and recovery times to gas exposure, rather than responding to it instantly. Due to this delay, and depending on the type of sensors, e-noses are often unable to achieve a steady state or provide a signal that is powerful enough to correctly identify the odor/gas being detected. This is still an open challenge [8, 67], while most olfactory robotic studies on odor classification are mostly based on pattern recognition in static or grounded robots.

2.3. Softgrowing robot applications

Most SGRs are a class of bio-inspired mechanical systems similar to vine plants in their growth-trailing behavior. The primary growing mechanism involves internal air pressure pushing material through the center of the robot's flexible, tubular body, turning it inside out at the tip in a process known as eversion. One advantage of this actuation process is that the robot's body extends forward without dragging or sliding against the environment, allowing it to access confined spaces with minimal friction [68].

Recently, the field of SGR has gained research interest in modeling, computational design, control, and applications. Models such as quasi-static kinematics have been applied to account for the robot's length, curvature, and bending stiffness to accurately predict growth and navigation parameters [69]. Motion planning, teleoperation, and vision-based autonomous steering have also been employed for smooth navigation during SGR operation [25, 37, 70]. This class of robots has proven its potential through various indoor and field demonstrations. Examples include navigating unknown environments using passive deformation [71], deploying distributed sensor networks to relay directional temperature and humidity data in hard-to-access spaces [72], exploring underground tunnels at archeological sites [25], investigating coral reefs [73], delivering tools and life support to trapped victims [32], operating as part of a cyber-physical measurement system [74], and clinical applications [75].

Although research on olfactory robotics continues to grow, to the best of our knowledge, no prior studies have specifically investigated odor identification and classification using SGRs. This is the first instance of a SGR being used for odor detection and the use of the collected data in a ML classification.

In this work, we introduce the concept of an *olfactory SGR*. SGRs possess unique advantages for olfactory tasks: they can elongate to significant lengths with minimal frictional interaction with their surroundings, they operate with fewer actuators than conventional mobile platforms, and they enable inherently safe, non-destructive exploration in confined or sensitive environments. They are also lightweight, moderately sized, and fabricated from low-cost, readily available materials [25, 26], making them more deployable than most rigid static or wheeled robots. The novelty of this work, therefore, lies in leveraging the intrinsic design properties of SGRs; their compliant growing mechanism, low mechanical complexity, and safe interaction characteristics, to enable a new modality of odor detection and classification that conventional robotic platforms cannot achieve.

Table I and Figure 3 provide a comparative description of our proposed olfactory SGR alongside previous olfactory robotic systems, based on key performance and design metrics. The static and wheeled/mobile systems shown in Cases 1 and 2 rely on conventional mechanical actuation and require

https://doi.org/10.1017/S0263574726103257 Published online by Cambridge University Press

Table I. *Comparison of olfactory robots based on key performance and design metrics.*

Criteria	Grounded/Static [5, 50]	Wheeled/Mobile [53, 54, 78]	Soft growing [25, 68, 79]
Environmental interaction	Moderate	High	Low
Actuator requirement	Moderate	High	Low
Workspace coverage	Limited	Moderate	High
Energy efficiency	High	Low–moderate	High
Payload capacity	High	Moderate	Low
Steering control	Simple	Moderate	High
Adaptive morphology	Low	Low	High

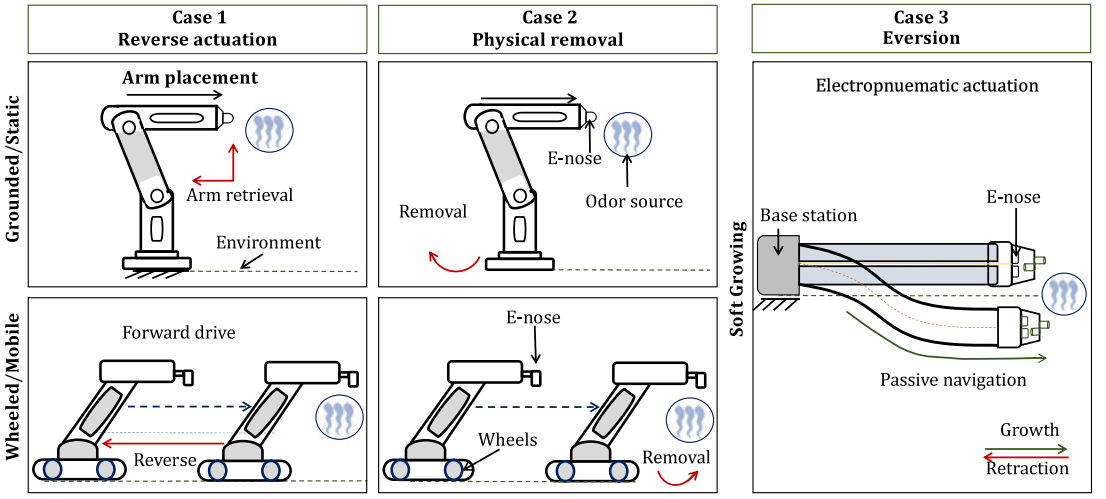


Figure 3. *Case 1 (left): Reverse actuation in static [5, 50], and mobile [53, 78]. For a static olfactory robot equipped with an actuated arm, the arm is simply driven in reverse to retrieve the e-nose after sampling. In mobile platforms, such as wheeled robots, retrieval may require retracing the traversal path to return the sensor to its origin. Case 2 (top and bottom): Physical removal of the system. In some static configurations, the entire robot or sampling assembly must be manually removed to recover the sensor. Likewise, mobile robots may need to be physically carried out of the environment if reverse traversal is impractical or unsafe. Case 3: Softgrowing robots. Inspired by vine-like tip growth, SGRs advance through tip eversion, enabling continuous odor data collection along the growth trajectory [68]. A single SGR can operate in both static and mobile scenarios using electropneumatic actuation for growth and retraction [25], while navigating either passively with minimal environmental contact or actively without requiring direct interaction with surrounding surfaces. This mechanism allows sensor deployment and gas removal [79] without traditional reverse motion or physical extraction.*

either reverse traversal or manual extraction for sensor retrieval. This is reflected in their higher actuator demands, greater environmental interaction, and limited adaptability [76, 77]. Static platforms exhibit restricted workspace coverage, while wheeled robots offer only moderate reach in confined environments due to locomotion constraints and the need to physically navigate the environment.

In contrast, the SGR in Case 3 shows more workspace coverage with minimal environmental contact, consistent with its tip-eversion mechanism that eliminates the need for backtracking or physical removal. Its low actuator requirement and high energy efficiency arise from pressurized eversion rather than jointed or wheel-based locomotion. Furthermore, the high adaptive morphology possible with SGRs enables reconfiguration and navigation in confined or irregular spaces – capabilities not achievable with rigid grounded or mobile platforms.

https://doi.org/10.1017/S0263574726103257 Published online by Cambridge University Press

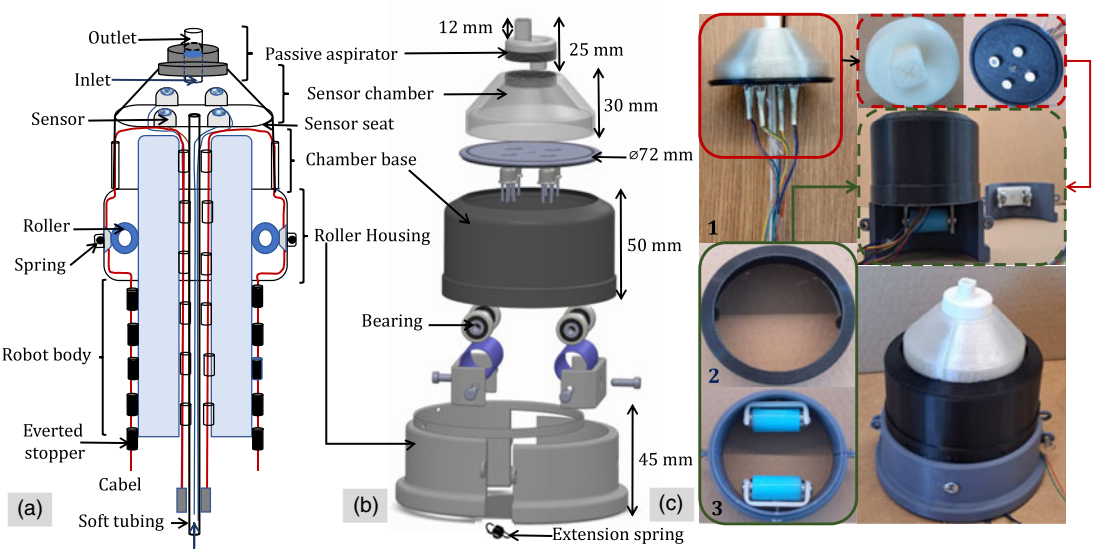


Figure 4. *Tip mount and sensor transporting mechanism. (a) Cross-sectional view (schematic) of the tip mount device installed on the inflated robot body. The robot body is mechanically coupled to the tip mount via side-tension cables, which pass through* 1 *cm slots located on both sides of the chamber base. These cables are redirected back toward the robot body and connected to motorized spools* M_2 *and* M_3*. Notably, the cable segments passing through the slots are unaffected by the stoppers, as the stoppers remain inverted within the robot tube during initial deployment, and are smaller than the slot diameter. As the robot everts, the stoppers, sensor wiring, and passive aspirator tube become exposed and extend outward. (b) CAD rendering of the exploded view, showing key components of the tip mount assembly along with dimensional references. (c) Subassembly and full assembly of the tip mount device. The system is modularly divided into three functional units: (1) The olfactory sensor module, (2) The coupling interface between the olfactory unit and the soft robot body, and (3) The device base, which houses the roller mechanism for growth and retraction control.*

In the following sections, we will implement this concept by developing the robotic system and evaluating its performance through static and transit odor detection experiments.

3. oSGR system description

In this section, we present the design of the robotic system and the sensor transportation mechanism. We detail the materials and methods employed to facilitate the robot's non-contact growth and orientation within its environment. In addition, we introduce the prototype, describing the design and mechanism of the tip mount, its characterization, and the aspiration technique; collectively enabling continuous sensor transport and olfactory sensing despite dynamic changes at the robot's tip. As an overview, our system uses three synchronized motorized spools: $M1$, $M2$, and $M3$. The main spool, $M1$ (Figure 1 *right*), holds the wound LDPE robot body and drives its eversion by unwinding it at a controlled speed. This motion is synchronized with $M2$ and $M3$ (Figure 1 *left*), which handle the release and retraction of pulling cables mechanically linked to the tip-mounted sensor mechanism (Figure 5). These cables help maintain the position and motion of the tip mount relative to the growing robot body. We then describe the materials and methods used to implement the system.

3.1. Robot design for non-contact eversion

This base station is a key component of the SGR system, often composed of a pressurized chamber housing the main spool, which directs the robot's orientation during eversion. There are two primary

https://doi.org/10.1017/S0263574726103257 Published online by Cambridge University Press

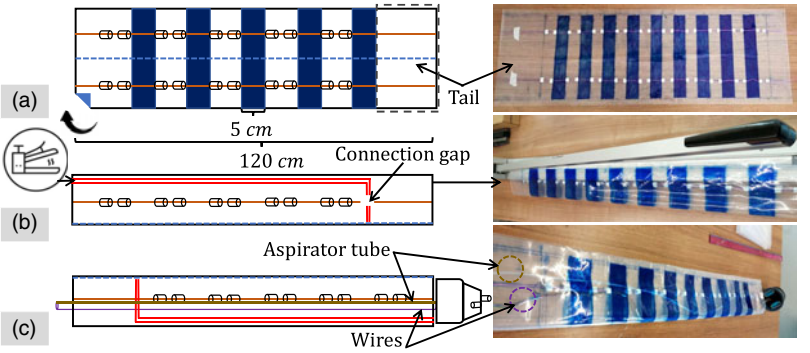


Figure 5. *Fabrication process of the olfactory SGR body. (a) An LDPE sheet is cut to* 120 *cm (*100 *cm growable length plus a* 20 *cm tail for the spool pulling cable), with* 5 *cm-wide tracking marks along its length. polytetrafluoroethylene tube stoppers (*1 *cm long,* 0.4 *cm diameter) are symmetrically positioned at* 2 *cm intervals using double-sided tape. Two pulling cables are passed through the stoppers for the tip mount support and navigation. (b) The sheet is sealed into a tube using an impulse heat sealer, leaving a* 0.6 *cm gap at the tail center for the passive aspirator tube and sensor wires. (c) The assembled tip mount device is fixed to the robot body by routing the aspirator tube and sensor wires from the tip through the body to the tail slot, where they pass from the base via a connector to the control unit.*

configurations for mounting the main spool: (i) vertical mounting of the spool directly onto the motor shaft, as in the design by Coad et al. [25], or (ii) horizontal mounting with actuation via a pulley–belt mechanism [80]. We opted for the first approach (Figure 1) for two reasons: (i) it enables direct and rapid rotation of the spool with minimal torque from the motor, and (ii) it allows the robot to grow mid-air through a vertical base without contacting its surroundings. This non-contact advantage is particularly relevant when transporting sensors or tools over sensitive environments. Our empirical tests show that the robot can extend up to 150 cm without collapsing when the tip mount is absent. However, in this study, we limited the operational length to 100 cm (Figure 5) due to the payload from the tip mount device. The vertical spool orientation also allowed us to characterize the buckling behavior induced by the tip mechanism under the robot's own weight.

As shown in Figure 1, the base is 3D-printed using polylactic acid and assembled in four parts: (i) the top seal, which houses the pneumatic check valve, connecting pins, and pressure sensor; (ii) the chamber, which stores compressed air and houses the inner spool with its electronic components; (iii) the actuation platform, located at the front of the cylinder, bearing housings for four brushless DC motors, connection circuits, and a small cylinder from which the everted LDPE tube grows; and (iv) the bottom seal. The seals are secured to the cylinder brim using silicone O-rings inserted into grooves, while the flanges are fastened with screws and nuts through 0.8 cm holes in the cylinder flange to provide reinforcement.

3.2. Fabrication of the soft-growing robot body

We fabricated the inflatable robot body as 8.5 cm diameter tube using flat LDPE sheets. We selected LDPE because of its low elastic modulus, high elongation at break, weldability, and suitability for pressure-driven eversion [26]. As described in Figure 5, we cut the flat sheet to a width of 31 cm and marked 2 cm sealing margins along both longitudinal edges, leaving a 27 cm central active region for inflation. To enable controllable tip bending, we integrated two symmetric pulling cables onto the sheet. We positioned the cables at a distance of 6.57 cm from each 2 cm sealing margin. With this configuration, the robot bends right or left when a differential compressive load is applied at the tip or when distributed loading accumulates along one side of the body. The cables also support the tip mount during eversion.

https://doi.org/10.1017/S0263574726103257 Published online by Cambridge University Press

We then routed the cables through polytetrafluoroethylene stoppers measuring 1 cm in length and 0.4 cm in diameter, spaced at 5 cm intervals. We secured each stopper to the LDPE sheet using double-sided adhesive tape to maintain precise cable alignment during eversion.

To form the pressurizable tube, we folded the sheet lengthwise onto itself with all stoppers enclosed and sealed the full length along the 2 cm margins using an impulse heat sealer. We also sealed the distal end of the tube, leaving a 0.6 cm central barrier to accommodate the folded sensor wires and the soft aspirator tube. After sealing, we removed the barrier, inserted the wires and tubing, and wrapped the tail tightly with tape (Gorilla weatherproof adhesive tape) to prevent air backflow during pressurization.

3.3. Tip mount design, mechanism, and evaluation

The material at the tip of SGR continuously changes as it grows and retracts; therefore, maintaining a tip mount that remains steadily fixed on the end effector is a significant challenge. Several designs in the literature have addressed this issue [38, 73, 81]. However, previous designs require embedding the entire tip mount drive system (whether motors or magnets) within the device, which limits optimal performance in non-contact eversion, particularly during mid-air operation. Motivated by this challenge, we developed a simplified tip-driven mechanism that relocates the drive components to the robot's base. This relocation not only reduces the payload at the tip but also improves growth dynamics and simplifies assembly, while preserving the stability of the tip mount during eversion and retraction. Figure 4 provides a detailed description of our tip mount mechanism, while Sections 3.3.1–3.3.4 present a characterization of its effects on the robot's eversion and navigation.

3.3.1. Growth and retraction modeling of the tip-mounted eversible robot

To describe the kinematics of our SGR with the tip-mounted assembly, we first model the interaction between pneumatic eversion and the mechanical resistance introduced by the roller-based mount and side-tension cable system. The geometric sketch is illustrated in Figure 6(a). During growth, the LDPE robot body everts outward through the tip, driven by internal pressure P. The net force applied to the interior surface of the tip mount is calculated from Eq. (1):

$$F_{\text{tip}} = P \cdot A, \ ; A = \pi r_i^2 \tag{1}$$

where A is the robot's area and r the radius.

For successful eversion, this force must exceed the combined resisting force F_f due to friction at the roller interface as given in Eq. (2):

$$F_{\text{tip}} > F_f = \mu_r \cdot N \tag{2}$$

where μ_r is the coefficient of friction between the Dycem-covered rollers and the robot body, and N is the normal preload applied by the extension springs. Once the frictional threshold is exceeded, the robot extends to length L at a rate governed by the supplied airflow over time $\dot{V}(t)$, with the resulting tip displacement given by Eq. (3):

$$\frac{dL(t)}{dt} = \frac{\dot{V}(t)}{\pi r_i^2} \tag{3}$$

As the robot continues to grow, the spring-loaded rollers conform passively to the robot's surface, maintaining grip while allowing smooth extension until the system approaches its burst pressure. The tip remains mechanically constrained within the rigid cap, generating a localized tension across the mount length. During retraction, the internal pressure is lowered by a pressure relief valve, and the motorized spool M_1 actively back-drives the body. Retraction occurs when the applied motor torque τ from M_1 overcomes the combined resistive torques from the robot's body tension and roller friction in Eq. (4):

$$\tau \geq r_s \cdot (T + F_f) \tag{4}$$

https://doi.org/10.1017/S0263574726103257 Published online by Cambridge University Press

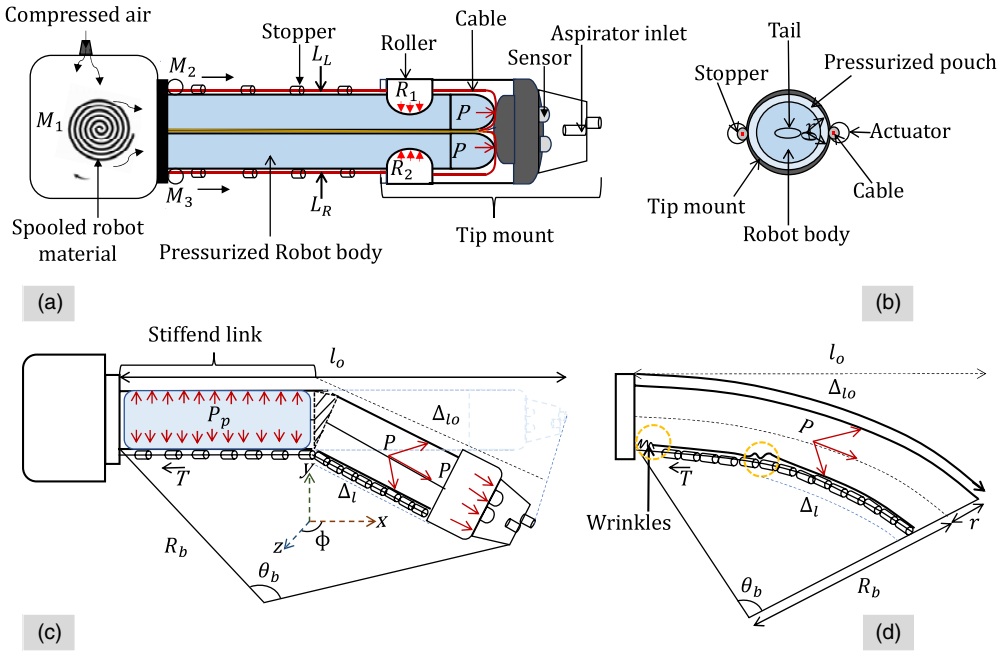


Figure 6. *Cross sections of the tip-mounted eversible robot. (a) Side axial cross-section of the robot. The robot body comprises a pressurized LDPE body, which resists deformation due to pressure-induced stiffness. Two cables (braided spectra lines) of lengths L_R on the right, and L_L on the left, run symmetrically along the robot body from external spools M_2 and M_3 to grooves at the rear of the tip mount. (b) Circumferential cross-section. The cables are routed through stoppers, which keep them aligned and create a contraction limit during bending. (c) Bending through active link stiffness (detailed in Section 3.3.2). The bending motion of the tip-mounted eversible robot is achieved through differential actuation, exploiting the geometry of the tip mount and the cables. When one cable is pulled while the other is released or held, asymmetric tension induces a curvature toward the tensed side. (d) Constant-curvature model of continuum-like robots.*

where r_s is the spool radius, and T is the longitudinal tension generated in the body and cables during retraction. The symmetric routing of the side cables ensures uniform retrieval unless differential actuation is introduced by motors M_2 or M_3.

To characterize the bending behavior of the robot under different mechanical configurations, we compare two distinct cases presented in Sections 3.3.2 and 3.3.3: (i) a segmented robot with selectively stiffened links (e.g., via inflated circumferential pouches) that localize deformation at discrete joints, and (ii) a continuously soft, pressurized beam without local stiffness modulation.

3.3.2. Stiffened link with localized bending

When SGRs are steered from the tip, the geometry is typically a curved segment with buckling at the base [82] (Figure 6(d)). One way to achieve selectively stiffened links and active segments is through layer jamming in a circumferential pouch [30, 34]. To model the mechanical behavior of our tip-mounted eversible robot for active bending without buckling at the base and desired link, we considered a nonlinear formulation that captures the gradual resistance introduced by the stoppers when the robot's tip is pulled.

https://doi.org/10.1017/S0263574726103257 Published online by Cambridge University Press

As the robot bends, the entire length changes by Δl_o, while the pulled cable shortens by a differential amount Δl (Figure 6(c) and (d)), and the contraction ratio is defined in Eq. (5) as:

$$a = \frac{\Delta l}{l_0} \tag{5}$$

where l_0 is the original length of the bending section. In the early stages of bending, adjacent stoppers do not make direct contact, and the system permits relatively free deformation. However, as bending increases, the stoppers begin to contact one another at a critical threshold defined by Eq. (6) [83]:

$$a_0 = \frac{l_g}{l_s + l_g} \tag{6}$$

where l_s and l_g represent the lengths of the stopper body and inter-stopper gap, respectively. Beyond this threshold, the stoppers compress against one another, introducing a nonlinear restoring force modeled in Eq. (7) as:

$$F_s(\Delta l) = \begin{cases} 0, & \Delta l < a_0 l_0 \\ k_s(\Delta l - a_0 l_0)^n, & \Delta l \geq a_0 L_0 \end{cases} \tag{7}$$

where k_s is the stiffness coefficient associated with the stopper material, and n is the empirical nonlinearity exponent. This stopper force contributes to the total torque that must be overcome for bending. To achieve or maintain the bend angle θ_b, we estimate the tension needed to hold or reach a specific bend angle θ_b, given a known internal pressure P and robot tube geometry (i.e., moment arm r).

Assuming the pulling cable exerts a tension T with an effective moment arm r, and the internal pressure P induces a resisting torque τ_P, the total torque balance (considering Eqs. (7) and (8)), is:

$$T = \frac{\tau_P}{r} + F_s(\Delta l) \tag{8}$$

Intuitively, from Eqs. (1) and (2), bending is initially governed by internal pressure and cable tension alone. However, in our design, the mechanical constraint imposed by the stoppers rapidly increases as the critical bend is approached, thereby defining the robot's maximum curvature. The nonlinear model provides a more realistic estimate of actuator force requirements for our tip-mounted eversible robot, and can be adjusted to match experimental bending force profiles by tuning k_s and n.

3.3.3. Non-segmented continuous bending

Non-segmented SGRs typically assume a constant-curvature model when actuated from the tip. Their behavior, both with tip-mounted steering systems [83, 84] and without [26, 82], has been extensively studied in prior work. A second case in our model shows the mechanical behavior for continuous bending with the spatially spaced stoppers and dual pulling cables along the robot body (Figure 6(d)).

Upon actuation, a tension T is applied to one of the cables, initiating bending from the tip. Unlike in the stiffened-link model (Section 3.3.2), this tension causes distributed curvature along the robot's length due to its compliant, pressurized structure. The stoppers act as constraint points, limiting relative displacement between adjacent points on the body. As the pulling continues, stoppers sequentially engage, accumulating local strain until adjacent stoppers at the joint reach the critical bending limit.

While the resistance torque still originates from the internal pressure P, it is now distributed along the body. The effective moment arm $\tilde{r}$, shorter than the robot's outer radius r, depends on the curvature distribution and local deformation shape. The tension required to achieve a given bend angle θ_b under this configuration can be approximated by Eq. (9) [85]:

$$T = \frac{|\tau_P|}{\tilde{r}} = \pi \tilde{r}^2 P \left(\tan^2 \left(\frac{\theta_b}{2} \right) + 1 \right) \tag{9}$$

From Eq. (9), and when compared to Eq. (8), it is obvious that a larger tension is required to achieve the same bend angle compared to the segmented robot in Figure 6(c) and Section 3.3.2. Nonetheless, the

https://doi.org/10.1017/S0263574726103257 Published online by Cambridge University Press

stopper–cable system acts to constrain and guide the deformation, enabling more predictable bending even in the fully non-segmented configuration.

3.3.4. Structural load analysis of tip mount assembly

The tip mount was designed to maintain a dynamic balance of forces during internal pressurization and actuation. The working pressure was empirically determined to ensure structural integrity while enabling mid-air eversion. It needed to be sufficient to both clamp the robot body to the rollers and support the tip-mounted device without inducing collapse. We found a pressure of 8.8 kPa to provide a reliable balance between these requirements. Upon inflation of the LDPE robot body, this internal pressure P produces a radially outward force against the inner tube wall, pressing it firmly against the rollers. This clamping effect increases the normal load N at the roller interface, thereby enhancing friction and improving grip between the robot body and the mount.

Given that the rollers have a diameter of 1.6 cm and a width of 3.8 cm, and that the tip mount assembly has a total mass of 86 g (with a length approximately 14% of the robot's fully extended length), the normal force was estimated using Eq. (1). Assuming A represents the effective contact area between the robot body and the rollers, the resulting radial force was computed as $F_{\text{rad}} = 1.77$ N.

In addition, we evaluated the structural integrity of the inflated LDPE tube under the gravitational load of the tip-mounted assembly by comparing the axial load W with the critical Euler buckling load P_{cr} for a fixed–free cantilevered column (Eq. 10):

$$P_{\text{cr}} = \frac{\pi^2 EI}{(KL)^2} \tag{10}$$

The parameters used were Young's modulus of LDPE $E = 200$ MPa; area moment of inertia computed from the hollow circular section with outer and inner diameters $D_o = 8.5$ cm and $D_i = 8.0$ cm, respectively; unsupported length $L = 100$ cm; and effective length factor $K = 2$ for a fixed–free column. The moment of inertia was obtained from Eq. (11):

$$I = \frac{\pi}{64}\left(D_o^4 - D_i^4\right) \tag{11}$$

yielding $I = 5.52 \times 10^{-7}$ m^4 for the specified geometry. Substituting these values into Eq. (10) results in a critical buckling load of $P_{\text{cr}} \approx 2.72 \times 10^2$ N.

Lastly, the axial gravitational load exerted by the mounted device was computed using Eq. (12):

$$W = m \cdot g \tag{12}$$

where $m = 0.086$ kg is the mass of the assembly and $g = 9.81$ m/s^2. This yields a downward load of $W = 0.84$ N. Since $W \ll P_{\text{cr}}$ (i.e., 0.84 n $\ll$ 272 N), the tube exhibits an extremely high safety margin against global Euler buckling under the applied load. It is worth noting that this Euler estimate is conservative: internal inflation pressure typically increases axial stability (pressure-stiffening), further enhancing resistance to buckling beyond the classical solid-column prediction.

3.4. Airflow through passive aspirator

In our olfactory SGR system, olfaction is enabled via a passive aspirator mounted at the extreme of the robot's tip mount (Figures 4 and 7). The aspirator inlet has a cross-sectional area $A_{\text{in}} = 1$ cm^2, a length of 1.2 cm, and operates under ambient room temperature ($T \approx 25$°C). It functions as a passive inlet, driven by pressure gradients generated by ambient airflow induced by a portable 5 V fan at maximum speed v_{fan}, and the robot's translational motion. We chose a single, well-defined inlet geometry to ensure that the passive aspirator entrains VOCs in a consistent flow pattern, thereby promoting uniform sample acquisition and enabling the generation of repeatable data across all exposure trials.

Under steady, incompressible flow conditions, the volumetric flow rate into the sensor chamber is approximated as (Eq. 13):

$$Q_{\text{asp}} = C_d A_{\text{in}} v_{\text{eff}} \tag{13}$$

https://doi.org/10.1017/S0263574726103257 Published online by Cambridge University Press

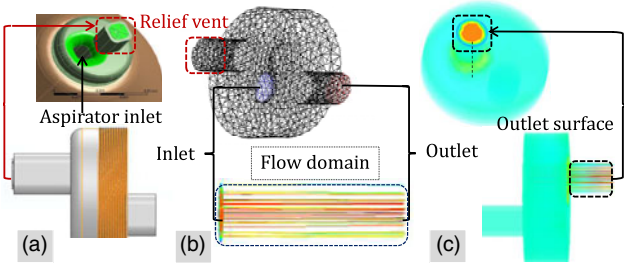


Figure 7. *(a) Side view of the main geometry. The passive aspirator features two inverted inlets and outlets for aspiration and relief. The aspiration inlet aligns with the floor of the connection platform and extends* 1.2 *cm into the sensor chamber. The relief inlet connects from inside the chamber to an outlet protruding* 1.5 *cm above the connection platform, sealed with a one-way silicone vent that opens under internal pressure. (b) Flow domain for fan-driven air inlet and outlet into the sensor chamber. (c) Volume renderings of airflow at the aspirator outlet into the sensor chamber, shown from top and side views.*

where $C_d \leq 1$ is the discharge coefficient (accounting for flow losses), and v_{eff} is the effective inlet velocity. During static operation, $v_{\text{eff}} \approx v_{\text{fan}}$. When the robot is in transit toward the VOC source at $v_{\text{transit}} \in \{0.05, 0.10\}$ m/s (as in the experiment), the effective inlet velocity is given in Eq. (14):

$$v_{\text{eff}} = v_{\text{fan}} + v_{\text{transit}} \tag{14}$$

This additive effect increases Q_{asp}, enhancing VOC sampling during transit. The transport of VOCs from the odor source to the aspirator inlet is governed by both advection and diffusion. Hence, assuming a well-mixed zone near the inlet, the VOC flux into the sensor chamber is expressed in Eq. (15):

$$J_{\text{VOC}} = Q_{\text{asp}}\, C_{\text{VOC}} \tag{15}$$

where C_{VOC} represents the local VOC concentration at the sampling point, which is influenced by the source emission rate E_{VOC}, environmental dispersion processes, and airflow patterns. The TGS-series sensors employed in the setup (TGS sensors 2600, 2602, 2611, and 2620) respond proportionally to the sampled VOC concentration [86]; that is Eq. (16):

$$S_{\text{sensor}} \propto C_{\text{VOC, sampled}} \tag{16}$$

With this proportionality, we assume that adsorption and desorption kinetics are sufficiently fast relative to the sampling timescales, ensuring a near-instantaneous sensor response to changes in VOC concentration. To relieve the sensor chamber of VOCs during the recovery phase, compressed air at high pressure is passed through the soft tube opening in the sensor chamber, as described in Figures 5 and 4. The other end of the tube, connected from inside the base to the pressure source, is sealed with a 0.4 cm check valve that prevents backflow of compressed air during the robot's operation. The flush pressure was regulated to 10 kPa in all experiments, flushing the air mixture out of the chamber via the forceful opening of the one-way relief vent shown in Figure 7(a).

3.5. Actuation control

The control system consists of a Faulhaber 3242X012BX4 3,692 brushless DC motor with an IER3-10000L encoder and a 20:1 gearbox paired with a Faulhaber MCBL3006 S RS driver to power the system (Figures 1 and 8). Motor actuation is managed through a 12-bit Dynomotion Kanalog-KFlop 8-axis controller board (Figure 8 (left)), using digital-to-analog commands. As discussed in Section 3.1, the electronic components in the base, including the pressure sensor end pins and motor driver cables, are connected to the controller with two 6 contact airtight wire connectors. The Dynomotion board communicates with the computer via a USB Type A-Type B cable. To achieve seamless eversion without slack in the response of the spool, we calculated the required speed at a pressure of 8.8 kPa, at which

https://doi.org/10.1017/S0263574726103257 Published online by Cambridge University Press

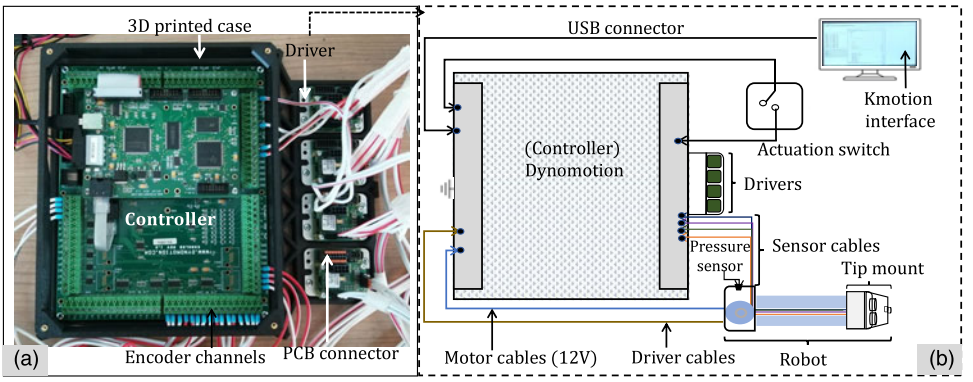


Figure 8. *(a) Dynomotion Kanalog-KFlop controller board with four motor drivers for the actuation (b) Schematics of the control unit for both the sensors and the robotic system using the Dynomotion Kanalog-KFlop controller board.*

new material is added to the tip when constrained by the mount rollers. We used an acceleration-based velocity control algorithm to determine this speed. First, we derived the controller derivation by defining the error function ϵ_v between the reference velocity $\dot{q}^{ref}$ and the response velocity $\dot{q}^{res}$ as in Eq. (17):

$$\epsilon_v = \dot{q}^{ref} - \dot{q}^{res}. \tag{17}$$

We then apply a first-order differential equation (Eq. 18) to force the error function to converge to zero and obtain the acceleration terms:

$$\dot{\epsilon}_v + k\epsilon_v = 0. \tag{18}$$

where k is a positive coefficient to ensure that the error converges to zero. Substituting Eq. (17) into Eq. (18) yields:

$$\ddot{q}^{ref} - \ddot{q}^{res} + k(\dot{q}^{ref} - \dot{q}^{res}) = 0. \tag{19}$$

Since our system has a disturbance observer structure [87], we can assume that all disturbances are compensated and that the response acceleration observed at the output of the system is the same as the input acceleration we provide to our system. Thus, the desired acceleration is obtained from Eq. (19) as follows:

$$\ddot{q}^{des} = \ddot{q}^{ref} + k(\dot{q}^{ref} - \dot{q}^{res}). \tag{20}$$

Eq. (20) describes the controller equation that provides the desired acceleration to the system, allowing it to follow the velocity reference. After configuring the motor speed, we applied a constant velocity reference of 0.57π rad/s and a voltage of 12 V to the motor driving the main spool M_1. This allowed the robot to extend up to 2 cm in 1 s at a pressure of 8.8 kPa.

3.6. Sensor description, experiment setup, and exposure timeline

The TGS sensors used in this study are the Figaro MOS TGS2600, TGS2602, TGS2611, and TGS2620 [86] shown in Figure 9(a). The sensors require two separate voltage inputs: the heater voltage (V_h) and the circuit voltage (V_c). The heater voltage V_h powers the built-in heating element, which maintains the sensing layer at an optimal operating temperature for VOC detection, while the circuit voltage V_c enables measurement of the output voltage (V_{out}) that varies with gas concentration [86]. Newly installed TGS sensors require continuous powering of the V_h for at least seven days to stabilize the baseline resistance and response characteristics of the sensing element. Hence, we connected, powered, and conditioned each sensor for a full 7-day period before calibration and experimental measurements commenced.

https://doi.org/10.1017/S0263574726103257 Published online by Cambridge University Press

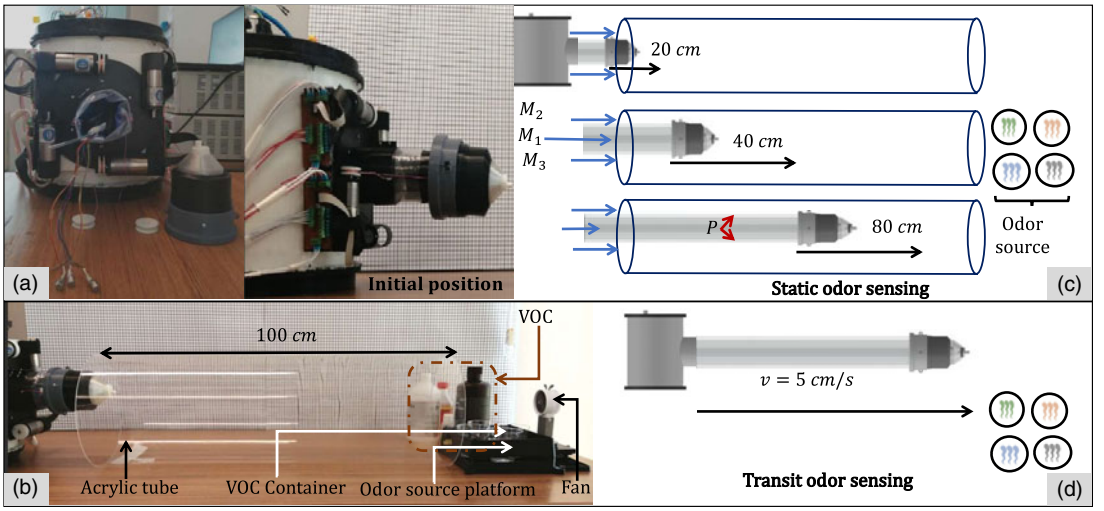


Figure 9. *Experimental setup. (a) Sensor array connections and passive aspirator tubing are integrated inside the fully retracted robot body. The assembly can be mounted directly onto the tip mount in its current position or positioned prior to retraction, as illustrated on the right. (b) Complete experimental setup comprising a* 100 *cm acrylic tube through which the robot everts, an odor-source platform holding four VOC containers, and a* 5 *V,* 5 *W fan to promote rapid volatile dispersion and improve sensor response time. (c) Static sensing: The robot advances toward the odor source at a constant speed of* 2 *cm/s, stopping at distances of* 20*,* 40*, and* 80 *cm for sampling. (d) Transit sensing: The robot traverses the VOC sources to a total length of* 100 *cm at actuation speeds of* 5 *cm/s and* 10 *cm/s, with continuous sensor data acquisition during motion.*

Furthermore, the sensors are analog gas sensors that output a voltage signal corresponding to the detected gas concentration. The sensor outputs, ranging from 0 to 5 V, were digitized using the 12-bit analog-to-digital converter (ADC) embedded within the controller described in Section 3.5. Since the voltage output varies with gas concentration, the resulting ADC values serve as an indirect measure of the gas levels detected by the robot.

As shown in Figure 9(b), the experimental platform consists of a transparent acrylic tube with an outer diameter of 25 cm and an inner diameter of 24 cm, through which our 8.5 cm diameter olfactory SGR was deployed. At the far end of the tube is a VOC source platform containing four cups, each filled with a different VOC: methane, ethanol, acetone, and gin. A portable 5 V, 5 W fan was positioned directly above the cups and operated at maximum speed to promote plume generation and dispersion along the tube. As discussed in Section 3.4, the robot's tip mount contains a passive aspirator that directs incoming air containing entrained VOCs into the sealed chamber housing the four gas sensors. All experiments were carried out at room temperature ($\approx 25^{\circ}$C). Figure 10 describes the experimental protocol, with the experiment trials as follows:

Experiment 1– *In-transit plus static sampling* (constant speed of $2cm/s$): Case 1: After the 20 s baseline, the robot moves for 10 s (20–30s), covering 20 cm, then stops to continue static sampling for the remaining 50 s (30–80 s). Static sampling occurs 80 cm from the odor source. Case 2: The robot moves for 20 s (20–40 s, 40 cm) before stopping, with static sampling at 60 cm from the source. Case 3: The robot moves for 40 s (20–60 s, 80cm), then samples statically at 20 cm from the source. Each experiment exposes the robot to a single VOC, recording responses from all four sensors. Repeating all VOCs across three distances results in 12 readings, each performed three times, totaling 36 samples.

Experiment 2 – *Full In-transit sampling:* Here, the robot moves continuously toward the 100 cm-distant VOC at 5 and 10 cm/s. After a 20 s baseline, it samples in-transit until reaching the source. Each VOC is tested separately, recording all sensor responses. Repeating for four VOCs at two speeds yields 8 readings, each repeated three times, totaling 24 samples.

https://doi.org/10.1017/S0263574726103257 Published online by Cambridge University Press

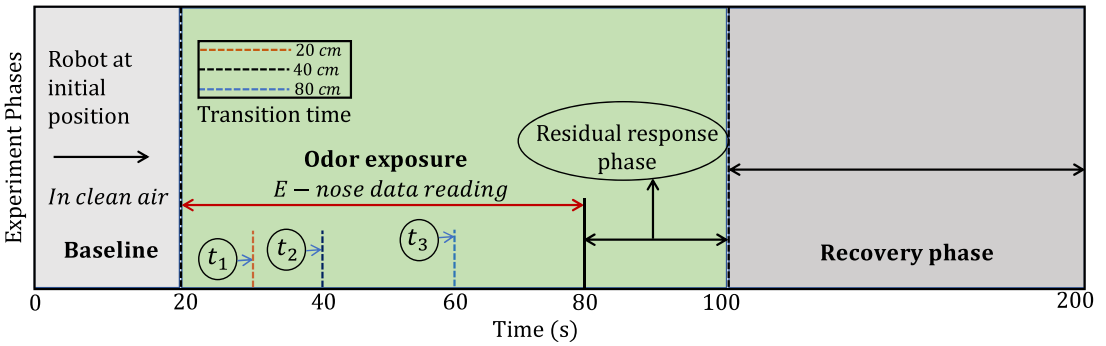


Figure 10. *Experimental timeline showing four sequential phases:* ***Baseline*** *(0–20 s): sensors stabilize in clean air with VOC containers sealed.* ***Exposure*** *(20–80 s): containers unsealed; odor sampling conducted under three in-transit + static distances – 20 cm ($t_1 = 10$ s transit + 50 s static), 40 cm ($t_2 = 20$ s transit + 40 s static), and 80 cm ($t_3 = 40$ s transit + 20 s static) – and two dynamic speeds (5 cm/s and 10 cm/s over 100 cm).* ***Residual response*** *(80–100 s): VOC sources resealed; sensors record lingering signal decay.* ***Recovery*** *(100–200 s): robot returns to clean air for full signal restoration before the next trial.*

4. Classification methodology

To assess the feasibility of integrating olfactory sensing into autonomous SGR platforms, we used the collected recordings to train a suite of supervised ML models. Datasets were acquired under five measurement conditions (three static standoffs at 20, 40, and 80 cm, and two dynamic transits at 5 and 10 cm/s), with three repetitions per odor source, giving 60 trials in total (Section 3.6). Each file contained time-series sensor voltages, which were processed entirely in Python (scikit-learn) with deterministic seeds for reproducibility. Figure 11 summarizes the overall pipeline.

To ensure consistent trial length for both training and real-time deployment, we chose a fixed analysis window of 20–100 s to exclude baseline and late recovery phases. For each sensor i, raw voltage $v_i(t)$ was baseline-corrected as given in Eq. (21)

$$x_i(t) = v_i(t) - \overline{v}_i^{[0,20]}, \tag{21}$$

where $\overline{v}_i^{[0,20]}$ is the mean output in the pre-exposure interval.

The resulting $x_i(t)$ were smoothed with a 1 s moving average filter. We then computed the training-set mean μ_i and standard deviation σ_i for each channel, and applied z-score normalization using Eq. (22). This ensures comparability across all sensors.

$$\tilde{x}_i(t) = \frac{x_i(t) - \mu_i}{\sigma_i}, \tag{22}$$

As shown in Figure 11, feature vectors $\mathcal{X}$ comprised the normalized time series $\tilde{x}_i(t)$ concatenated across all four sensors over $t \in [20, 100]$ s, augmented with summary descriptors (peak amplitude, exposure integral, recovery slope, and time-over-threshold). Labels $\mathcal{Y}$ were assigned at the trial level.

In addition, we split the dataset into training/validation/testing subsets (60/20/20), stratified by odor type to maintain class balance. Hyperparameter tuning was performed via 5-fold cross-validation on the training set (Figure 12), and final models were evaluated on the held-out test set.

Specifically, twelve classifiers frequently applied in gas-sensing literature were benchmarked, including k-Nearest Neighbor (KNN) [88], Random Forest Classifier (RFC) [89], Gradient Boosting Classifier (GBC) [90], Decision Tree Classifier (DTC) [91], LightGBM Classifier (LGBMC) [92], Multi-Layer Perceptron Classifier (MLPC) [93], Support Vector Classifier (SVC) [94], Logistic Regression (LR) [95], Stochastic Gradient Descent Classifier (SGDC) [90], Linear Discriminant Analysis (LDA) [96], Gaussian Naive Bayes (GNB) [97], and Multinomial Naive Bayes (MNB) [98]. Performance was assessed using accuracy, macro-averaged precision, recall, and F1-score [99].

https://doi.org/10.1017/S0263574726103257 Published online by Cambridge University Press

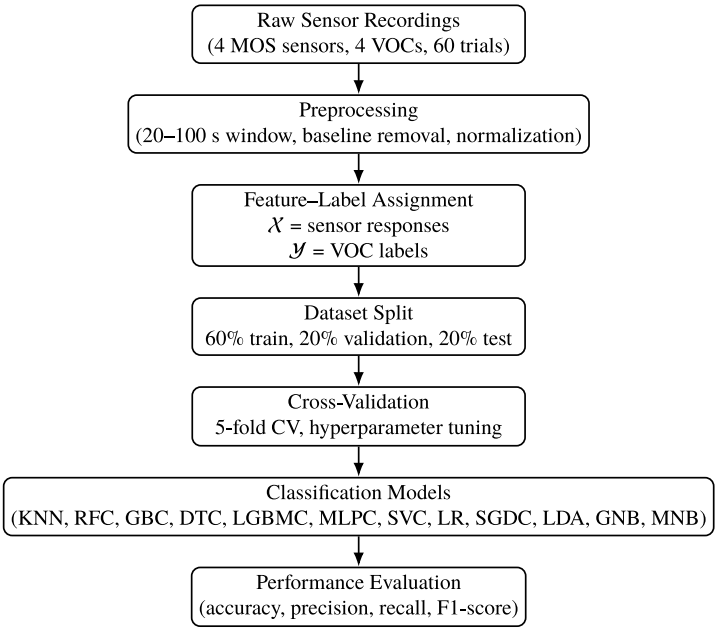


Figure 11. *Block diagram of the machine-learning methodology. Raw olfactory recordings from the four TGS sensors were preprocessed, segmented, and merged into a labeled dataset. Features and labels were extracted, followed by reproducible train/validation/test splits and k-fold cross-validation. Twelve supervised learning algorithms were trained and benchmarked on the dataset to evaluate odor classification performance under both static and dynamic experimental conditions.*

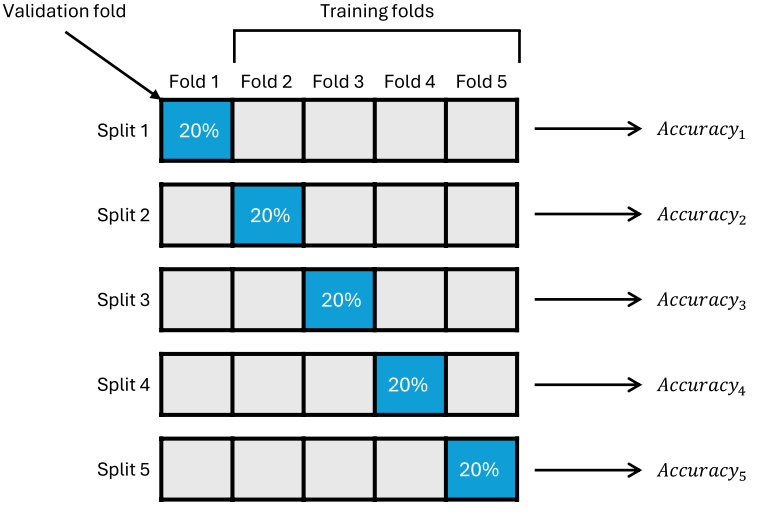


Figure 12. *Illustration of $k = 5$ cross-validation. Each fold is used once for validation, while the remaining $k - 1$ folds are used for training. This reduces variance in validation error estimates and guides hyperparameter selection.*

5. Demonstrations, experiments, and results

In this section, we demonstrate the olfactory sensing capabilities of our proposed SGR system using the prototype of the tip mount device. First, as illustrated in Figure 13 *left*, we evaluated the pneumatic

https://doi.org/10.1017/S0263574726103257 Published online by Cambridge University Press

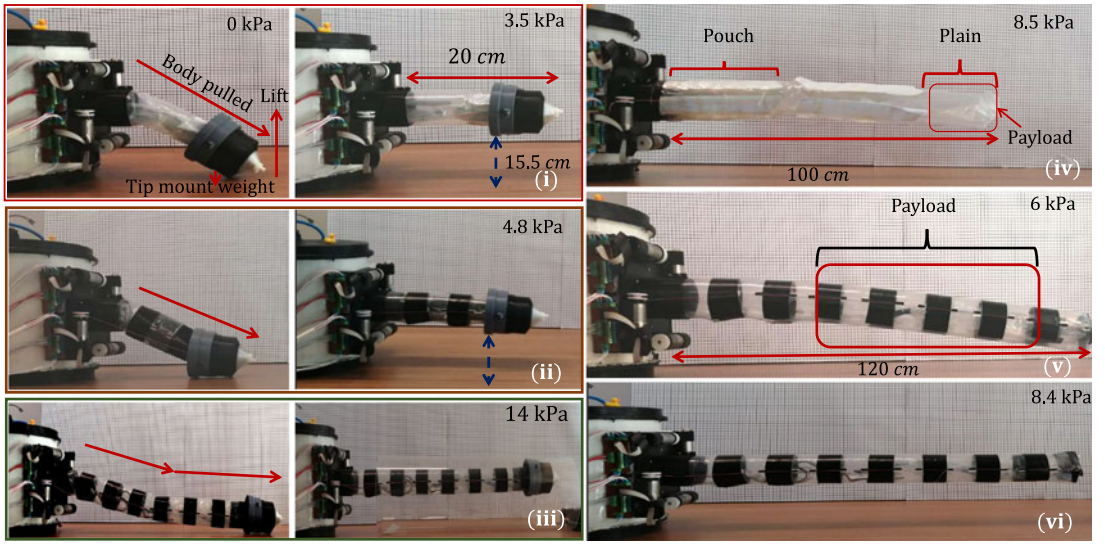


Figure 13. *Demonstrations.* ***(Left and center)****: Tip-mounted pulling of the robot body at* 0 *kPa, and corresponding lift pressures for (i) the pouch body at* 20 *cm, and the non-pouched body at (ii)* 20 *cm and (iii)* 100 *cm.* ***(Right)****: Payload influence on (iv) the pouch-embedded robot body at* 100 *cm length, and (v; vi) the payload and maximum lift pressure required in the non-pouch body at* 120 *cm length.*

behavior of the robot under varying configurations, including (i) the robot's ability to lift the tip-mounted payload against gravity at two body lengths (20 cm and 100 cm) using both a plain body and a pouch-embedded variant and (ii) the robot's full eversion behavior while carrying the tip mount (Figure 13 *right*). The results are presented in Figure 14(a) and (b). Second, we conduct two distinct olfactory experiments using the same prototype. The first experiments, illustrated in Figure 15, involve the robot (i) everting into a simulated pipe environment toward four VOC sources located 100 cm away at the far end, while collecting odor data without contacting the inner pipe walls, and (ii) traversing directly over the odor source at a constant speed of 5 cm/s and 10 cm/s. We designed the last two setups to emulate the signal acquisition process of an e-nose system mounted on a grounded robot, or a mobile robot as it moves closer, passes near, or directly over a gas source.

5.1. Pneumatic eversion under varying configurations

The pressure dynamics of the SGR during growth were systematically evaluated under varying mechanical configurations to assess the influence of payload and actuation strategy on the system performance. As a baseline, we first measured the pneumatic requirement for a plain robot without any tip-mounted device. In this case, the pressure required for minimal growth was 2.1 kPa, increasing steadily along the growth trajectory and stabilizing at approximately 6 kPa for full extension to 100 cm (Figure 14(a)). Subsequently, we evaluated three configurations with the tip-mount device: (i) all three motors (M_1, M_2, and M_3) active; (ii) only the central motor M_1 active, with M_2 and M_3 disabled; and (iii) with embedded pouches. When all three motors were active, the initial pressure requirement was 4.2 kPa, rising steadily to 9 kPa at full extension. In contrast, operating only the central motor produced the steepest pressure curve, with the requirement increasing from 6 kPa at minimal growth to approximately 14 kPa at full length. The lack of lateral mechanical support in this configuration led to asymmetric loading, higher drag, and reduced eversion efficiency. Finally, in the embedded pouch configuration, the initial pressure was higher (5.8 kPa) due to the added mass of the pouch assembly; however, the peak pressure during growth dropped to 11.5 kPa, with the pressure curve flattening earlier in the trajectory compared to the central-motor-only scenario.

https://doi.org/10.1017/S0263574726103257 Published online by Cambridge University Press

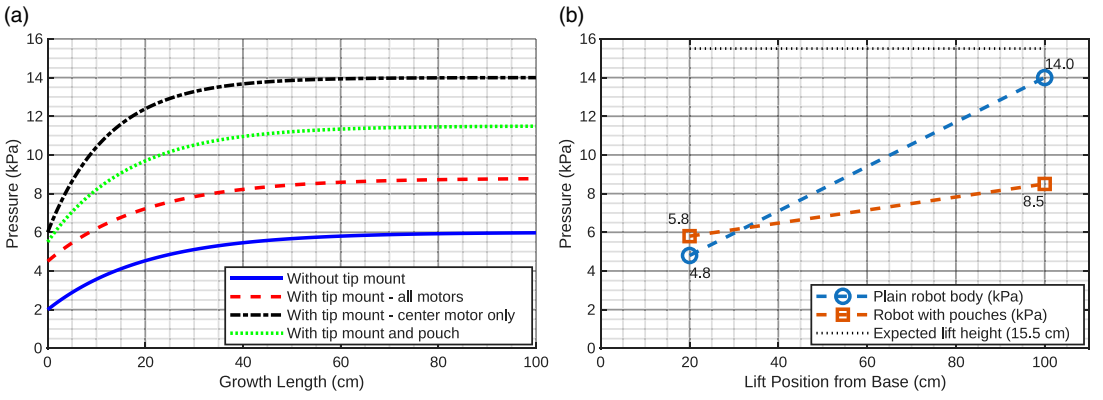


Figure 14. *(a) Pressure dynamics for various growth configurations to understand how payload influences the performance of the robotic system (b) pressure needed to vertically lift the robot's tip-mounted payload at heights of* 20 *cm and* 100 *cm, while comparing plain and pouch-embedded bodies.*

Figure 14(b) shows the pressure needed to vertically lift the robot's tip-mounted payload at two heights of 20 cm and 100 cm, comparing the two body types. In the plain body, pressure rises sharply from 4.8 kPa at 20 cm to 14.0 kPa at 100 cm, indicating an increasingly demanding lift due to cumulative gravitational torque. On the other hand, the pouch-enhanced, sectioned body offers better load support for the second section (plain), resulting in higher initial pressure (5.8 kPa), due to added material weight, but lower pressure at full lift (8.5 kPa) compared to the fully plain body.

5.2. Static and transit sensing

Figure 15 shows the oSGR prototype during the experiments. In both Experiments 1 and 2, all four sensors produced their strongest responses to at least one of the four target gases, while also exhibiting measurable cross-sensitivities to non-target gases. This behavior is consistent with the broad spectral width and overlapping response bands of tin-oxide–based sensors, where the observed signals reflect a mixture of selective and non-selective interactions. We explicitly consider these characteristics in the design of the classification models.

Figure 16 presents sensor responses in Experiment 1 under combined in-transit and static sampling at three distances. In case 1 (*left*), corresponding to short transit (10 s) and long static exposure (50 s), the robot began sampling VOCs after the 20 s baseline period, advanced for 10 s (20–30 s), and then continued static sampling for 50 s. Case 2 (*middle*) represents moderate transit and static exposure: the robot extended 40 cm over 20 s (20–40 s) before pausing for a 40 s static phase (40–80 s). Case 3 (*right*) depicts extended transit and short static exposure, where the robot advanced for 40 s (20–60 s) and stopped at a 20 cm standoff.

As shown in Figure 16(a–d), response magnitudes were strongly monotonic with distance. Closer standoffs consistently produced higher peak amplitudes, faster rise times, and longer durations above threshold. For instance, 80 cm growth (20 cm standoff) yielded the largest signals, whereas 20 cm growth (80 cm standoff) produced the weakest. Although decay constants were broadly similar across distances, stronger peaks resulted in proportionally larger residual signals, suggesting that higher exposures slowed complete desorption. Sensor-specific differences were also evident: ethanol and gin elicited the largest responses on TGS2602 and TGS2620, methane responses were strongest on TGS2611, and acetone produced moderate but consistent activity on TGS2602 and TGS2620.

In Experiment 2, we extended the sequence of olfactory tasks to investigate the effect of traversal speed (5 cm/s, solid lines; 10 cm/s, dashed lines) on sensor array performance. As in Experiment 1, baseline signals remained stable until exposure (Figure 17(a–d)). However, unlike static sampling, these

https://doi.org/10.1017/S0263574726103257 Published online by Cambridge University Press

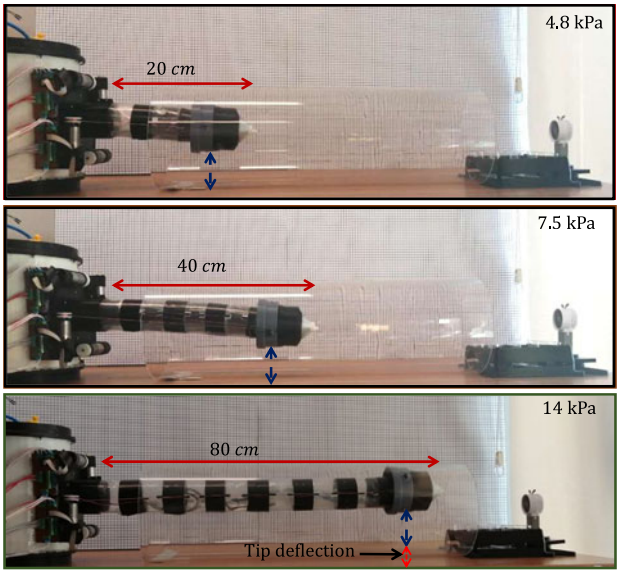


Figure 15. *VOC sampling experiments. The robot grows to lengths of* 20 *cm,* 40 *cm, and* 80 *cm toward the VOC source at a constant speed of* 2 *cm/s, without contacting the pipe walls. The blue arrow beneath the tip mount indicates its height above the inner floor of the pipe. In the* 80 *cm experiment (bottom), a smaller red arrow beneath the blue highlights the change in tip mount height caused by the increased pressure required to counteract the payload at the tip.*

trials exhibited compressed exposure windows due to reduced residence time in the high-concentration zone. The resulting responses were more transient, with narrower peaks and sharper decays. A clear speed-dependent effect emerged: runs at 10 cm/s consistently showed narrower temporal profiles than 5 cm/s, while peak amplitudes remained broadly comparable across sensor–gas pairs.

At the level of individual sensors, Experiment 2 reproduced the patterns observed in Experiment 1, although with compressed dynamics. TGS2611 again showed the strongest selectivity to methane, with distinct exposure and recovery phases that mirrored its dominant role in Experiment 1. TGS2602 and TGS2620 produced the highest responses to ethanol and gin, with peak magnitudes comparable to static cases but faster post-exposure decay. Acetone responses remained moderate on TGS2602 and TGS2620 and weak on TGS2600 and TGS2611, similar to Experiment 1. Importantly, the overall ranking of sensor–gas sensitivities was preserved across both experiments, indicating that traversal speed primarily affected the temporal shape of response curves without altering the relative selectivity of the sensor array.

6. Supervised machine-learning-based classification

Figure 18 presents a statistical summary of the raw dataset, computed over the 100-second window corresponding to the sensors' active response phase. The boxplots display standard metrics, including Q1 (first quartile), the value below which 25% of readings fall and represents the lower bound of the response distribution; Q2 (median), the dataset's midpoint; and Q3 (third quartile), the value below which 75% of readings fall. To further assess inter-sensor relationships, a correlation heatmap was generated, as shown in Figure 19(a).

The supervised ML results for all tested classifiers are summarized in Table II. In this task, variants of the odor dataset were presented to each model to identify the VOC present (see the ML workflow in the supplementary file). Among the twelve classifiers evaluated, the KNN algorithm achieved the highest performance, with an accuracy of 99.88% and equally strong precision, recall, and F1-scores across all odor classes. This consistency highlights its robustness in distinguishing between the VOCs in

https://doi.org/10.1017/S0263574726103257 Published online by Cambridge University Press

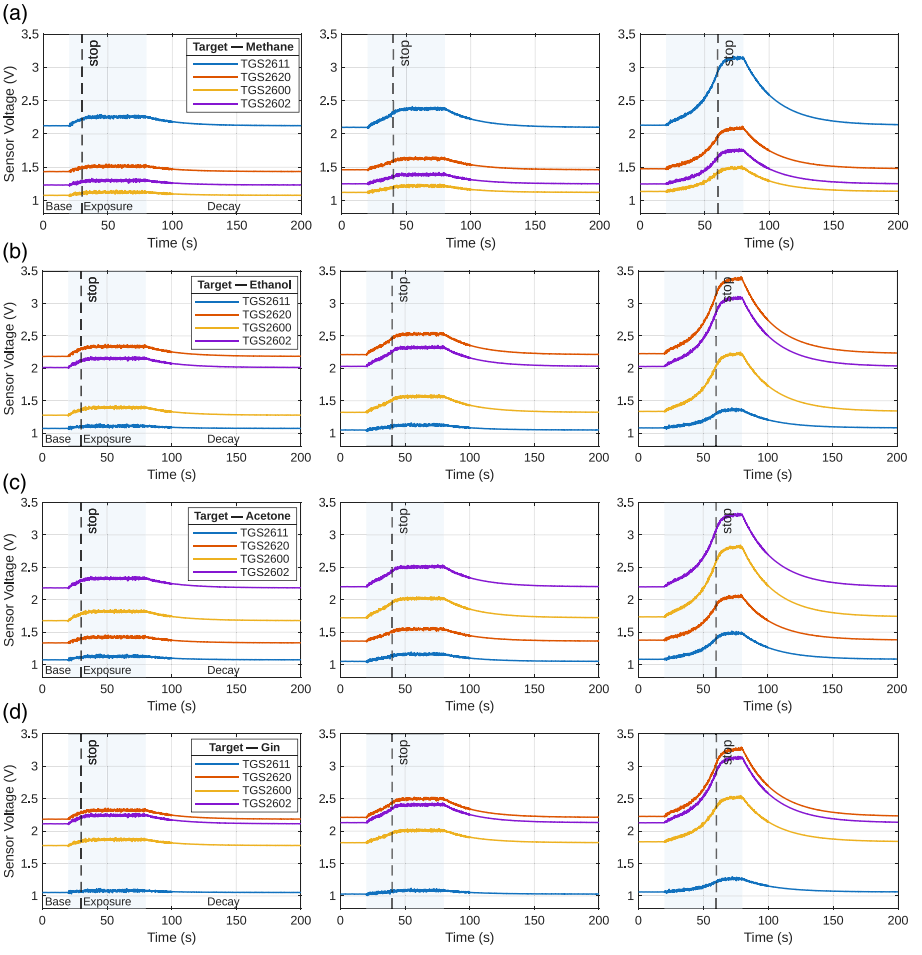


Figure 16. *Experiment 1 showing sampling responses of all four sensors at three different exposure intervals: (left) t_1: 10 s in-transit followed by 50 s static, (middle) t_2: 20 s in-transit followed by 40 s static, and (right) t_3: 40 s in-transit followed by 20 s static. Readings were recorded during exposure to methane, ethanol, gin, and acetone (a–d), respectively.*

our dataset. LGBMC followed closely with an accuracy of 99.22%, while ensemble methods such as the RFC and DTC also performed strongly, achieving 99.43% and 98.32%, respectively. By comparison, SVC and LR models, although still achieving good accuracies of 95.59% and 93.93%, were less effective in capturing the full complexity of the odor signal patterns.

We further assessed the performance of the KNN classifier using a confusion matrix, which visualizes the model's ability to correctly assign each odor sample to its corresponding class (Figure 19(b)). For instance, accurate classification of acetone occurs when the model predicts "acetone" for an acetone sample (true positive) and avoids incorrectly labeling it as another gas (false positive/false negative). In this context, the sensor readings are represented as feature vectors, and the KNN algorithm determines the class by identifying the k nearest neighbors in the feature space and assigning the majority class among them. As shown in Figure 19, the model achieved 97.76% accuracy for acetone, 98.99% for ethanol (with 1.01% misclassifications), 99.12% for gin (with 0.88% misclassifications), and 100% accuracy for methane with no errors, confirming the model's strong discriminative capability across all sampled VOCs.

https://doi.org/10.1017/S0263574726103257 Published online by Cambridge University Press

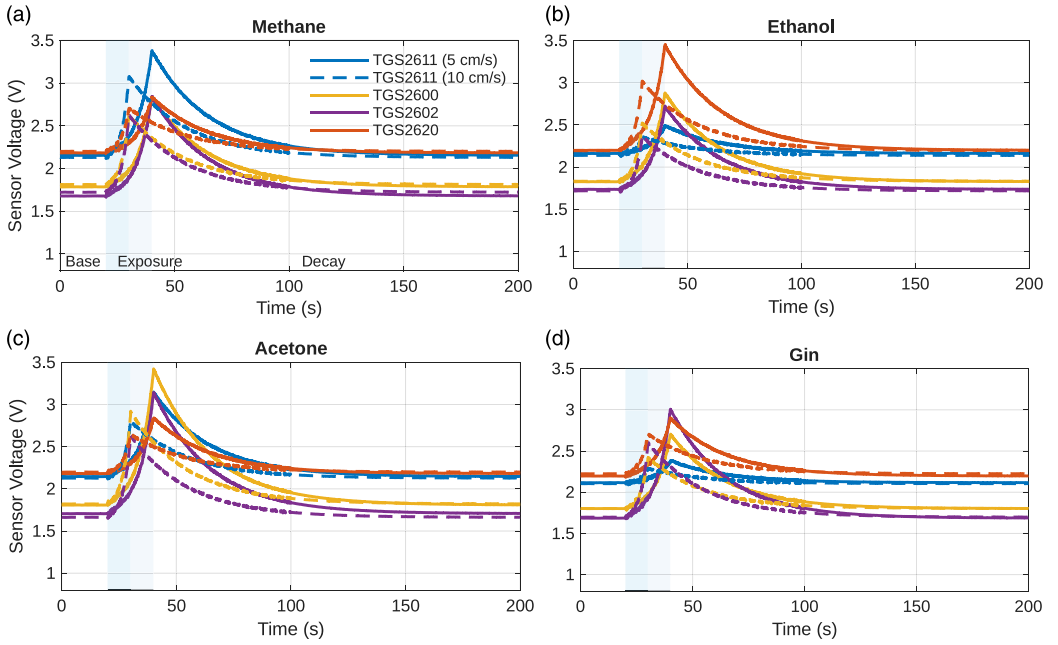


Figure 17. *Experiment 2: Sampling responses of the four TGS sensors at two different exposure speeds;* 5 ***cm/s (solid lines) and*** 10 *cm/s (dashed lines), during exposure to methane, ethanol, gin, and acetone (a–d), respectively. The legend colors correspond to the same sensors as shown in experiment 1.*

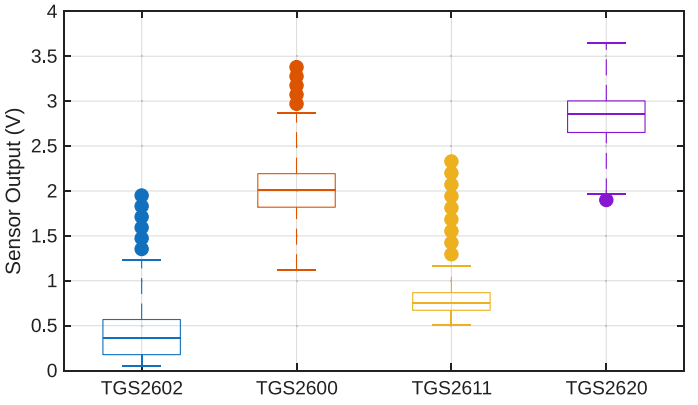


Figure 18. *Sensor output distributions during the entire odor exposure for the four gas sensors. Each box illustrates the interquartile range between the first quartile (Q1) and third quartile (Q3), with the horizontal line inside the box indicating the median (Q2). The whiskers extend to the minimum and maximum recorded values during the exposure period. TGS2600 and TGS2620 show relatively higher mean and median values compared to TGS2602 and TGS2611, reflecting stronger baseline signal levels during exposure. In the context of our ML pipeline, these distributions highlight sensor-specific signal characteristics that influence feature separability, directly impacting classifier performance and robustness in the odor classification tasks.*

7. Discussion

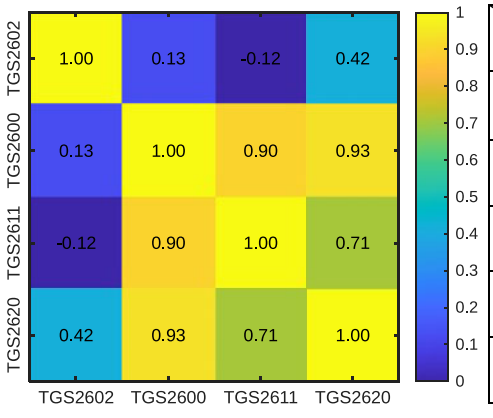
As discussed in Section 2.3, our olfactory SGR system is designed to achieve non-contant eversion through a medium slightly larger than its body diameter (Figure 13). To enable the robot's motion on the ground, the base can be oriented horizontally, thereby changing the rotational axes of the motorized spools M_1, M_2, and M_3 from axial to radial. As illustrated in Figure 13, coordinated actuation of the

https://doi.org/10.1017/S0263574726103257 Published online by Cambridge University Press

Table II. *Odor classification performance metrics for different tested ML models.*

Model type	Accuracy (%)	F1 Score (%)	Precision (%)	Recall (%)
KNN	99.88	99.88	99.88	99.88
RFC	99.43	99.43	99.43	99.44
GBC	99.34	99.39	99.39	99.40
DTC	98.32	98.32	98.34	98.34
LGBMC	99.22	99.22	99.22	99.23
MLPC	96.60	96.61	96.66	96.64
SVC	95.59	95.61	95.67	95.65
LR	93.93	93.99	94.11	94.01
SGDC	85.88	85.69	85.70	86.07
LDA	80.73	81.29	83.78	80.75
GNB	72.55	74.04	77.41	72.66
MNB	66.26	66.08	66.37	66.68

(a)



(b)

Target / Output	Acetone	Ethanol	Gin	Methane	Σ
Acetone	1264 24.94%	3 0.06%	26 0.51%	0 0.00%	1293 97.76% 2.24%
Ethanol	2 0.04%	1279 25.24%	11 0.22%	0 0.00%	1292 98.99% 1.01%
Gin	11 0.22%	0 0.00%	1243 24.53%	0 0.00%	1254 99.12% 0.88%
Methane	0 0.00%	0 0.00%	0 0.00%	1229 24.25%	1229 100.00% 0.00%
Σ	1277 98.98% 1.02%	1282 99.77% 0.23%	1280 97.11% 2.89%	1229 100.00% 0.00%	5015 / 5068 98.95% 1.05%

Figure 19. *(a) Correlation heatmap showing relationships between readings from the four sensors for each classified odor. Positive values indicate proportional changes, negative values indicate inverse relationships, and diagonal values (1.00) represent perfect self-correlation. TGS2600 and TGS2620 exhibit a strong positive correlation (0.93), as do TGS2600 and TGS2611 (0.90). A moderate correlation exists between TGS2602 and TGS2620 (0.42), while TGS2611 and TGS2602 show a weak negative correlation (−0.12). (b) Confusion matrix of the KNN classifier, with prediction accuracies of 100% for methane, 99.12% for gin, 98.99% for ethanol, and 97.76% for acetone.*

three motors enables eversion, which can also provide passive and active two-dimensional tip steering. Furthermore, three-dimensional bending can be achieved via auxiliary actuators positioned on the upper and lower sections of the actuator platform (Figure 1). Consequently, the robot can perform tasks such as obstacle avoidance and adaptive search. In contrast, achieving similar functionality with wheeled sniffers [6] or rigid mobile robots [6, 52], as shown in Figure 3, typically requires multiple distributed actuators and complex kinematic controls, leading to increased system complexity.

Unlike previous tip-mount designs that embed motors or employ magnetic stabilization mechanisms [32], our tip-mount design architecture reduces system complexity by relocating all actuation components to the robot's base (Figure 1). This base-driven configuration minimizes the tip payload, thereby: (i) improving growth dynamics. As shown in Figure 13, the robot body successfully lifted the tip mount payload both at a short extension of 20 cm and at a full length of 100cm, requiring only 4.8kPa and 14kPa of internal pressure, respectively; and (ii) simplifying assembly. The system is modularly divided

https://doi.org/10.1017/S0263574726103257 Published online by Cambridge University Press

into three functional units (Figure 4), enabling the tip mount device to be attached or removed without detaching the robot body or disconnecting the wound sensor assembly (Figure 9a) from the base outlet. In addition, decoupling the motorized rollers or magnetic system from the tip allows substantial miniaturization of the tip mount device, as its design is no longer constrained by motor housing dimensions. This approach complements prior studies that have demonstrated sub-centimeter-scale SGR designs [31, 100].

Furthermore, with regard to the olfactory sensors (e-nose), the mechanical and structural design of our system readily supports the integration of additional or alternative sensors. In the current configuration, each TGS sensor weighs less than 30g [86], and the complete tip-mounted assembly supports a payload of 0.84 n under an internal pressure of only 8.8 kPa – well below the measured burst threshold of 14 kPa. Many modern sensors, such as the Bosch BME688 (1.7 g), AMS CCS811 (0.9 g), and Sensirion SGP40 (0.6g) [101–103], are significantly lighter and more compact than traditional TGS devices. The modular 3D-printed tip cap can be easily reconfigured with custom sensor seats to accommodate different form factors, and the weight constraint remains flexible as long as the aggregate mass is below the supported payload limit.

As noted in Section 3.4, the experimental protocol was inspired by biological olfactory sampling and designed to emulate active sampling during the approach to an odor plume. Our experimental results (Figure 16) confirm that, unlike conventional systems that separate locomotion and sensing, the olfactory SGR performs continuous odor sampling throughout eversion. Because sensing and growth are co-located at the tip and occur concurrently, the robot acquires concentration information at every stage of deployment without stopping or mechanical reconfiguration. This continuous sampling strategy reduces detection latency and reduces energy expenditure associated with repeated repositioning, a notable advantage over rigid mobile platforms and wheeled sniffers that must frequently halt to resample [104]. One notable finding from the eversion characterization is that the embedded pouch configuration shows how strategic payload integration can offset the initial mass penalty by lowering peak pressure requirements during sustained growth. This capability is particularly important for scaling the system to longer range, where minimizing pneumatic load directly translates into reduced energy consumption and improved operational efficiency.

To evaluate the utility of the experimental olfactory dataset (Figure 16 and Section. 5.2), we implemented an ML classification pipeline with twelve supervised classifiers (Section. 4), to assess discrimination of the VOCs. The kNN model achieved the highest performance, with 99.88% accuracy and recall across all test conditions (Table II). Although this result highlights the potential of kNN as a key component in future autonomous olfactory SGRs, given its robustness and high classification accuracy, its detection accuracy and reliability, especially in complex or unpredictable odor landscapes, would be a focus of future work.

Our results demonstrate that raw olfactory data from the growing robot is inherently separable across multiple VOC classes, even under varying motion and exposure conditions. The cross-sensitivity patterns observed across VOCs and sensors remained consistent between experiments, indicating that the same ML classifiers can be applied to both static and dynamic scenarios when temporal features such as rise and recovery times are considered. This confirms that the sensing modality is stable and discriminative enough to support ML-driven classification without hardware or sampling modifications, while also establishing the current setup as a reliable platform for generating training data. Practically, this enables future robot iterations to integrate on-board classification for context-aware behaviors such as adjusting growth direction, modulating sampling speed, or initiating retraction based solely on live sensor input. Thus, the ML results not only validate post-processing performance but also demonstrate that the olfactory SGR platform is ready for real-time, closed-loop operation.

Although the proof-of-concept evaluation in this work was conducted within a linear (1D) pipe environment, prior studies have already established the ability of SGRs to passively conform to and navigate complex 2D and 3D pipe networks [105]. These demonstrations confirm that the underlying locomotion modality is inherently compatible with branched, curved, and spatially varying conduits. Consequently, the present study focuses primarily on characterizing the proposed olfactory sensing architecture and

https://doi.org/10.1017/S0263574726103257 Published online by Cambridge University Press

validating its operational feasibility through a controlled, simplified deployment scenario. To take advantage of our non-contact tip design in such environments, future implementations can integrate real-time shape sensing (e.g., soft strain sensors) and proprioceptive feedback to track the robot's configuration within the pipe network. Coupled with onboard or remote mapping algorithms, this would enable autonomous path planning in branched and curved channels while maintaining continuous odor sampling. For teleoperated scenarios, the compact tip and reduced drag of our design can be combined with intuitive control interfaces (e.g., haptic feedback joysticks) to allow operators to guide the robot through highly convoluted geometries without physical contact with the pipe walls. However, there is a critical length beyond which the robot will collapse under its own weight [106], and transporting tools or sensors over long distances magnifies this risk. The low-friction, non-contact eversion in our design helps reduce bending stress and wall-induced drag, thereby delaying – but not eliminating – this collapse threshold. One way to address this limitation could be through optimized inflation pressure or intermediate support mechanisms, especially to extend the operational reach of the system in realistic 2D and 3D tasks.

8. Conclusion and future work

This work introduces the concept of an *o*SGR as a novel extension of tip-eversion–based robotic technology. The research was organized around four primary objectives: (i) achieving stable, non-contact eversion; (ii) designing a lightweight, motorized tip-mount device for secure and adaptable sensor positioning; (iii) acquiring experimental olfactory data in both static and dynamic operational scenarios; and (iv) validating the use of this data for ML-based odor classification. All objectives were successfully achieved. The robot demonstrated stable eversion over a 100 cm reach without collapse; the tip mount securely transported the sensor array during growth while enabling passive aspiration; the VOC sampling was consistently recorded in all experiments; and twelve ML classifiers were evaluated, the kNN model achieving the highest performance (99.88% accuracy and recall).

Beyond meeting these objectives, the results highlight that combining tip growth and non-contact eversion with an integrated olfactory sensing module allows the system to overcome operational challenges commonly faced by rigid or wheeled robots in confined, sensitive, or hazardous environments. The raw olfactory data collected during growth were inherently separable across odor classes, even under varying source proximities and approach dynamics. Furthermore, the ability to sense continuously without halting for dedicated sampling reduced both detection latency and operational energy consumption, offering a clear advantage over conventional stop-and-sense approaches.

A current limitation lies in the rigidity of the tip mount, which prevents deformation through apertures smaller than the robot's diameter – an otherwise characteristic advantage of SGRs. Addressing this limitation through the development of soft or morphing tip designs is a priority for future work, as it would broaden the range of accessible environments. Furthermore, while the use of a passive aspirator in this study may be less efficient than active pumping systems in terms of odor acquisition, it successfully demonstrated the feasibility of consistent and repeatable VOC sampling during continuous in-motion operation, enabled for the first time in SGR platform by our tip-mounted sensor design. Incorporating an active pump at the tip of an SGR, particularly without environmental contact to provide counter-support, presents significant design and weight-distribution challenges, which warrant further investigation. Finally, building on the success of this proof-of-concept, our future research will explore integrating the robot's maneuverability with on-board ML inference, enabling autonomous leak detection and multi-gas monitoring in inaccessible, unstructured and hazardous environments.

Author contributions. Investigation, A.J.O., and A.A.; data curation, A.J.O., A.A., U.A.Y., G.K., and F.S.; visualization, A.J.O., and A.A.; writing – original draft preparation, A.J.O., A.A., and F.S.; writing – review and editing, A.J.O., A.A., E.A.B., and F.S.; supervision, E.A.B. and F.S.; funding acquisition, F.S. All authors have read and agreed to the published version of the manuscript.

Financial support. This work is funded by TUBİTAK within the scope of the 2,232-B International Fellowship for Early Stage Researchers Program number 121C145.

https://doi.org/10.1017/S0263574726103257 Published online by Cambridge University Press

Competing interests declarations. The authors declare that they have no conflicts of interest regarding the publication of this paper.

Data availability statement. The machine learning code for this work is publicly available at https://github.com/evolabpc/odor-classification.

Ethical standards. Not applicable.

References

[1] X.-X. Chen and J. Huang, "Odor source localization algorithms on mobile robots: A review and future outlook," *Robot. Auton. Syst.* **112**(1), 123–136 (2019).

[2] H. Ishida, T. Nakamoto, T. Moriizumi, T. Kikas and J. Janata, "Plume-tracking robots: A new application of chemical sensors," *Biol. Bull.* **200**(2), 222–226 (2001).

[3] J. G. Monroy, J.-L. Blanco and J. Gonzalez-Jimenez, "Time-variant gas distribution mapping with obstacle information," *Auton. Robot.* **40**(1), 1–16 (2016).

[4] A. D. Wilson, "Applications of electronic-nose technologies for noninvasive early detection of plant, animal and human diseases," *Chemosensors* **6**(4), 45 (2018).

[5] A. J. Moshayedi, A. S. Khan, Y. Shuxin, G. Kuan, H. Jiandong, M. Soleimani and A. Razi, "E-Nose design and structures from statistical analysis to application in robotic: A compressive review," *EAI Endorsed Trans. AI Robot.* **2**(1), e1 (2023).

[6] M. Abdelkhalek, S. Alfayad, F. Benouezdou, M. B. Fayek and L. Chassagne, "Compact and embedded electronic nose for volatile and non-volatile odor classification for robot applications," *IEEE Access* **7**, 98267–98276 (2019).

[7] J. Monroy, J.-R. Ruiz-Sarmiento, F.-A. Moreno, C. Galindo and J. Gonzalez-Jimenez, "Olfaction, vision, and semantics for mobile robots. Results of the IRO project," *Sensors* **19**(16), 3488 (2019).

[8] M. Trincavelli, S. Coradeschi and A. Loutfi, "Classification of Odours with Mobile Robots Based on Transient Response," **In:** *International Conference on Intelligent Robots and Systems* (IEEE/RSJ, 2008) pp. 4110–4115.

[9] G. Reddy, V. N. Murthy and M. Vergassola, "Olfactory sensing and navigation in turbulent environments," *Annu. Rev. Condens. Matter Phys.* **13**(1), 191–213 (2022).

[10] L. Marques, A. Martins and A. T. de Almeida, "Environmental Monitoring with Mobile Robots," **In:** *International Conference on Intelligent Robots and Systems* (IEEE/RSJ, 2005) pp. 3624–3629.

[11] S. Soldan, G. Bonow and A. Kroll, "RoboGasInspector – A mobile robotic system for remote leak sensing and localization in large industrial environments: Overview and first results," *FAC Proc., Vol.* **45**(8), 33–38 (2012).

[12] J. P. H. Steele, Q. Han, H. Karki, K. Al-Wahedi, A. A. Ayoade, M. R. Sweatt, D. P. Albert and W. A. Yearsley, "Development of an Oil and Gas Refinery Inspection Robot," **In:** *ASME International Mechanical Engineering Congress and Exposition*, vol. **46476** (American Society of Mechanical Engineers, 2014) pp. V04AT04A016.

[13] J. Monroy, J.-R. Ruiz-Sarmiento, F.-A. Moreno, F. Melendez-Fernandez, C. Galindo and J. Gonzalez-Jimenez, "A semantic-based gas source localization with a mobile robot combining vision and chemical sensing," *Sensors* **18**(12), 4174 (2018).

[14] Y. Choi, K. Kim, S. Kim and D. Kim, "Identification of odor emission sources in urban areas using machine learning-based classification models," *Atmos. Environ.: X* **13**, 100156 (2022).

[15] G. C. H. E. de Croon, L. M. O'connor, C. Nicol and D. Izzo, "Evolutionary robotics approach to odor source localization," *Neurocomputing* **121**, 481–497 (2013).

[16] J. Wang, Y. Lin, R. Liu and J. Fu, "Odor source localization of multi-robots with swarm intelligence algorithms: A review," *Front. Neurorobot.* **16**, 949888 (2022).

[17] H. Fan, E. Schaffernicht and A. J. Lilienthal, "Ensemble learning-based approach for gas detection using an electronic nose in robotic applications," *Front. Chem.* **10**, 863838 (2022).

[18] H. G. J. Voss, J. J. A. Mendes Júnior, M. E. Farinelli and S. L. Stevan Jr., "A prototype to detect the alcohol content of beers based on an electronic nose," *Sensors* **19**(11), 2646 (2019).

[19] L. Wang and S. Pang, "Robotic odor source localization via adaptive bio-inspired navigation using fuzzy inference methods," *Robot. Auton. Syst.* **147**, 103914 (2022).

[20] V. H. Bennetts, A. J. Lilienthal, P. P. Neumann and M. Trincavelli, "Mobile robots for localizing gas emission sources on landfill sites: Is bio-inspiration the way to go?," *Front. Neuroeng.* **4**, 20 (2012).

[21] B. Zhang, Y. Fan, P. Yang, T. Cao and H. Liao, "Worm-like soft robot for complicated tubular environments," *Soft Robot.* **6**(3), 399–413 (2019).

[22] Y. Zhao, H. Huang, W. Yuan, X. Liu and C. C. Cao, "Worm-inspired, untethered, soft crawling robots for pipe inspections," *Soft Robot.* **11**(4), 639–649 (2024).

[23] X. Liu, M. Song, Y. Fang, Y. Zhao and C. Cao, "Worm-inspired soft robots enable adaptable pipeline and tunnel inspection," *Adv. Intell. Syst.* **4**(1), 2100128 (2022).

[24] W. Zhao, Y. Zhang and N. Wang, "Soft robotics: Research, challenges, and prospects," *J. Robot. Mechatron.* **33**(1), 45–68 (2021).

[25] M. M. Coad, L. H. Blumenschein, S. Cutler, J. A. R. Zepeda, N. D. Naclerio, H. El-Hussieny, U. Mehmood, J.-H. Ryu, E. W. Hawkes and A. M. Okamura, "Vine robots," *IEEE Robot. Autom. Mag.* **27**(3), 120–132 (2019).

https://doi.org/10.1017/S0263574726103257 Published online by Cambridge University Press

[26] L. H. Blumenschein, M. M. Coad, D. A. Haggerty, A. M. Okamura and E. W. Hawkes, "Design, modeling, control, and application of everting vine robots," *Front. Robot. AI* **7**, 548266 (2020).
[27] H. El-Hussieny, I. A. Hameed and A. B. Zaky, "Plant-inspired soft growing robots: A control approach using nonlinear model predictive techniques," *Appl. Sci.* **13**(4), 2601 (2023).
[28] M. Yu, W. Liu, J. Zhao, Y. Hou, X. Hong and H. Zhang, "Modeling and analysis of a composite structure-based soft pneumatic actuators for soft-robotic gripper," *Sensors* **22**(13), 4851 (2022).
[29] F. Stroppa, "Design optimizer for planar soft-growing robot manipulators," *Eng. Appl. Artif. Intel.* **130**, 107693 (2024).
[30] I. Exarchos, K. Wang, B. H. Do, F. Stroppa, M. M. Coad, A. M. Okamura and C. K. Liu, "Task-specific Design Optimization and Fabrication for Inflated-beam Soft Robots with Growable Discrete Joints," **In:** *International Conference on Robotics and Automation (ICRA)* (IEEE, 2022) pp. 7145–7151.
[31] C. Girerd, A. Alvarez, E. W. Hawkes and T. K. Morimoto, "Material scrunching enables working channels in miniaturized vine-inspired robots," *IEEE Trans. Robot.* **40**, 2166–2180 (2024).
[32] S. G. Jeong, M. M. Coad, L. H. Blumenschein, M. Luo, U. Mehmood, J. H. Kim, A. M. Okamura and J. H. Ryu, "A Tip Mount for Transporting Sensors and Tools Using Soft Growing Robots," **In:** *International Conference on Intelligent Robots and Systems (IROS)* (IEEE//RSJ, 2020) pp. 8781–8788.
[33] B. H. Do, S. Wu, R. R. Zhao and A. M. Okamura, "Stiffness change for reconfiguration of inflated beam robots," *Soft Robot.* **11**(5), 779–790 (2024).
[34] B. H. Do, V. Banashek and A. M. Okamura, "Dynamically Reconfigurable Discrete Distributed Stiffness for Inflated Beam Robots," **In:** *International Conference on Robotics and Automation (ICRA)* (IEEE, 2020) pp. 9050–9056.
[35] M. L. Dezaki, M. Bodaghi, A. Serjouei, S. Afazov and A. Zolfagharian, "Soft pneumatic actuators with controllable stiffness by bio-inspired lattice chambers and fused deposition modeling 3d printing," *Adv. Eng. Mater.* **25**(6), 2200797 (2023).
[36] J. D. Greer, L. H. Blumenschein, R. Alterovitz, E. W. Hawkes and A. M. Okamura, "Robust navigation of a soft growing robot by exploiting contact with the environment," *Int. J. Robot. Res.* **39**(14), 1724–1738 (2020).
[37] F. Stroppa, M. Luo, K. Yoshida, M. M. Coad, L. H. Blumenschein and A. M. Okamura, "Human Interface for Teleoperated Object Manipulation with a Soft Growing Robot," **In:** *International Conference on Robotics and Automation* (IEEE, 2020) pp. 726–732.
[38] F. Stroppa, M. Selvaggio, N. Agharese, M. Luo, L. Blumenschein, E. H. Hawkes and A. M. Okamura, "Shared-control teleoperation paradigms on a soft-growing robot manipulator," *J. Intell. Robot. Syst.* **109**, 30 (2023).
[39] H. El-Hussieny and I. Hameed, "Obstacle-aware navigation of soft growing robots via deep reinforcement learning," *IEEE Access* **12**, 38192–38201 (2024).
[40] A. Ataka and A. P. Sandiwan, "Growing Robot Navigation Based on Deep Reinforcement Learning," **In:** *International Conference on Control, Automation and Robotics (ICCAR)* (IEEE, 2023) pp. 115–120.
[41] W. Huang, P. Li, Z. Zhang, Z. Wang, D. Zhou and L. Li, "Goal-oriented control strategies for soft growing robots," *IEEE Robot. Autom. Lett.* **10**(10), 9886–9893 (2025).
[42] C. Watson, R. Obregon and T. K. Morimoto, "Closed-loop position control for growing robots via online jacobian corrections," *IEEE Robot. Autom. Lett.* **6**(4), 6820–6827 (2021).
[43] A. Kalibala, A. A. Nada, H. Ishii and H. El-Hussieny, "Real-time force/position control of soft growing robots: A data-driven model predictive approach," *Nonlinear Eng.* **14**(1), 20250099 (2025).
[44] C. Zanchettin, L. M. Almeida and F. D. de Menezes, "An intelligent monitoring system for natural gas odorization," *IEEE Sens. J.* **15**(1), 425–433 (2014).
[45] A. H. Jalal, F. Alam, S. Roychoudhury, Y. Umasankar, N. Pala and S. Bhansali, "Prospects and challenges of volatile organic compound sensors in human healthcare," *ACS Sens.* **3**(7), 1246–1263 (2018).
[46] A. Pomerantz, R. Blachman-Braun, J. A. Galnares-Olalde, R. Berebichez-Fridman and M. Capurso-García, "The possibility of inventing new technologies in the detection of cancer by applying elements of the canine olfactory apparatus," *Med. Hypotheses* **85**(2), 160–172 (2015).
[47] H. Li, J. A. Covington, F. Tian, Z. Wu, Y. Liu and L. Hu, "Development and analysis of an artificial olfactory bulb," *Talanta* **279**, 126551 (2024).
[48] L. Cheng, Q.-H. Meng, A. J. Lilienthal and P.-F. Qi, "Development of compact electronic noses: A review," *Meas. Sci. Technol.* **32**(6), 062002 (2021).
[49] A. P. D. Heredia, F. R. Cruz, J. R. Balbin and W.-Y. Chung, "Olfactory Classification Using Electronic Nose System Via Artificial Neural Network," **In:** *Region 10 Conference (TENCON)* (IEEE, 2016) pp. 3569–3574.
[50] J. Gonzalez-Jimenez, J. G. Monroy and J. L. Blanco, "The multi-chamber electronic nose – an improved olfaction sensor for mobile robotics," *Sensors* **11**(6), 6145–6164 (2011).
[51] P. Maho, C. L. Dolcinotti, T. Livache, C. Herrier, A. Andreev, P. Comon and S. Barthelme, "Olfactive Robot for Gas Discrimination Over Several Months Using a New Optoelectronic Nose," **In:** *International Symposium on Olfaction and Electronic Nose (ISOEN)* (IEEE, 2019) pp. 1–3.
[52] H. Harianto, M. Rivai and D. Purwanto, "Implementation of electronic nose in omni-directional robot," *Int. J. Electr. Comput. Eng.* **3**(3), 399 (2013).
[53] Y. Xing, T. A. Vincent, H. Fan, E. Schaffernicht, V. H. Bennetts, A. J. Lilienthal, M. Cole and J. W. Gardner, "Firenose on mobile robot in harsh environments," *IEEE Sens. J.* **19**(24), 12418–12431 (2019).
[54] H. Fan, V. H. Bennetts, E. Schaffernicht and A. J. Lilienthal, "Towards gas discrimination and mapping in emergency response scenarios using a mobile robot with an electronic nose," *Sensors* **19**(3), 685 (2019).

https://doi.org/10.1017/S0263574726103257 Published online by Cambridge University Press

[55] F. Piqué, F. Stella, J. Hughes, E. Falotico and C. D. Santina, "Smell Driven Navigation for Soft Robotic Arms: Artificial Nose and Control," **In:** *International Conference on Soft Robotics (RoboSoft)* (IEEE, 2023) pp. 1–7.

[56] J. Burgués, L. F. Valdez and S. Marco, "High-Bandwidth E-Nose for Rapid Tracking of Turbulent Plumes," **In:** *International Symposium on Olfaction and Electronic Nose (ISOEN)* (IEEE, 2019) pp. 1–3.

[57] M. Liu, Y. Zhang, J. Wang, N. Qin, H. Yang, K. Sun, J. Hao, L. Shu, J. Liu, Q. Chen, P. Zhang and T. H. Tao, "A star-nose-like tactile-olfactory bionic sensing array for robust object recognition in non-visual environments," *Nat. Commun.* **13**(1), 79 (2022).

[58] C. Sanchez-Garrido, J. G. Monroy and J. Gonzalez-Jimenez, "A Configurable Smart E-Nose for Spatio-Temporal Olfactory Analysis," **In:** *SENSORS* (IEEE, 2014) pp. 1968–1971.

[59] M. Rasekh, H. Karami, A. D. Wilson and M. Gancarz, "Classification and identification of essential oils from herbs and fruits based on a MOS electronic-nose technology," *Chemosensors* **9**(6), 142 (2021).

[60] S. Sankaran, L. R. Khot and S. Panigrahi, "Biology and applications of olfactory sensing system: A review," *Sens. Actuators B: Chem.* **171**, 1–17 (2012).

[61] L. H. Nyayu, A. S. Handayani, S. Nurmaini and I. Yani, "Odor Classification Using Support Vector Machine," **In:** *International Conference on Electrical Engineering and Computer Science (ICECOS)* (IEEE, 2017) pp. 87–91.

[62] D. Yan, H. Cao, P. Zhang and S. Yang, "Fuzzy linguistic odor cognition for robotics olfaction," *IEEE Trans. Cogn. Devel. Syst.* **11**(2), 234–243 (2018).

[63] S. Li, L. Feng, Y. Ge, L. Zhu and L. Zhao, "An ensemble learning method for robot electronic nose with active perception," *Sensors* **21**(11), 3941 (2021).

[64] S. Hassan, L. Wang and K. R. Mahmud, "Robotic odor source localization via vision and olfaction fusion navigation algorithm," *Sensors* **24**(7), 2309 (2024).

[65] K. Fukuyama, K. Matsui, S. Omatsu, A. Rivas and J. M. Corchado, "Feature Extraction and Classification of Odor Using Attention Based Neural Network," **In:** *International Conference of Distributed Computing and Artificial Intelligence* (Springer, 2020) pp. 142–149.

[66] R. Kausar, F. Zayer, J. Viegas and J. Dias, "Efficient Hybrid Neuromorphic-Bayesian Model for Olfaction Sensing: Detection and Classification," **In:** *International Conference on Robotics and Automation (ICRA)* (IEEE, 2024) pp. 2089–2095.

[67] J. G. Monroy and J. Gonzalez-Jimenez, "Gas classification in motion: An experimental analysis," *Sens. Actuators B: Chem.* **240**, 1205–1215 (2017).

[68] E. W. Hawkes, L. H. Blumenschein, J. D. Greer and A. M. Okamura, "A soft robot that navigates its environment through growth," *Sci. Robot.* **2**(8), eaan3028 (2017).

[69] C. Tutcu, B. A. Baydere, S. K. Talas and E. Samur, "Quasi-static modeling of a novel growing soft-continuum robot," *Int. J. Robot. Res.* **40**(1), 86–98 (2021).

[70] Z. Wu, S. M. Hadi Sadati, K. Rhode and C. Bergeles, "Vision-based autonomous steering of a miniature eversion growing robot," *IEEE Robot. Autom. Lett.* **8**(11), 7841–7848 (2023).

[71] F. Fuentes and L. H. Blumenschein, "Mapping Unknown Environments Through Passive Deformation of Soft, Growing Robots," **In:** *International Conference on Intelligent Robots and Systems (IROS)* (IEEE/RSJ, 2023) pp. 2522–2527.

[72] A. M. Gruebele, A. C. Zerbe, M. M. Coad, A. M. Okamura and M. R. Cutkosky, "Distributed Sensor Networks Deployed Using Soft Growing Robots," **In:** *International Conference on Soft Robotics (RoboSoft)* (IEEE, 2021) pp. 66–73.

[73] J. Luong, P. Glick, A. Ong, M. S. DeVries, S. Sandin, E. W. Hawkes and M. T. Tolley, "Eversion and Retraction of a Soft Robot Towards the Exploration of Coral Reefs," **In:** *2019 2nd IEEE International Conference on Soft Robotics (RoboSoft)* (IEEE, 2019) pp. 801–807.

[74] S. Grazioso, A. Tedesco, M. Selvaggio, S. Debei and S. Chiodini, "Towards the development of a cyber-physical measurement system (CPMS): Case study of a bioinspired soft growing robot for remote measurement and monitoring applications," *Acta IMEKO* **10**(2), 104–110 (2021).

[75] A. J. Oyejide, F. Stroppa and M. Saraç, "Miniaturized soft growing robots for minimally invasive surgeries: Challenges and opportunities," *Prog. Biomed. Eng.* **7**(3), 033001 (2025).

[76] J. He and F. Gao, "Mechanism, actuation, perception, and control of highly dynamic multilegged robots: A review," *Chin. J. Mech. Eng.* **33**(1), 79 (2020).

[77] B. He, S. Wang and Y. Liu, "Underactuated robotics: A review," *Int. J. Adv. Robot. Syst.* **16**(4), 1729881419862164 (2019).

[78] M. A. Arain, V. H. Bennetts, E. Schaffernicht and A. J. Lilienthal, "Sniffing out fugitive methane emissions: Autonomous remote gas inspection with a mobile robot," *Int. J. Robot. Res.* **40**(4-5), 782–814 (2021).

[79] S. Lee, N. G. Kim, D. Seo, S. Park and J.-H. Ryu, "Helical Structured Soft Growing Robot for Hazardous Gas Suction in Inaccessible Environments," **In:** *2025 IEEE International Conference on Robotics and Automation (ICRA)* (IEEE, 2025) pp. 12907–12913.

[80] U. Hofmann, M. Fankhauser, S. Willen, D. Inniger, C. Klahn, K. Löffel and M. Meboldt, "Design of an additively manufactured hydraulic directional spool valve: An industrial case study," *Virtual Phys. Prototyp.* **18**(1), e2129699 (2023).

[81] J. D. Greer, T. K. Morimoto, A. M. Okamura and E. W. Hawkes, "A soft, steerable continuum robot that grows via tip extension," *Soft Robot.* **6**(1), 95–108 (2019).

[82] H. El-Hussieny, I. A. Hameed and J.-H. Ryu, "Nonlinear model predictive growth control of a class of plant-inspired soft growing robots," *IEEE Access* **8**, 214495–214503 (2020).

[83] R. Jitosho, S. Simón-Trench, A. M. Okamura and B. H. Do, "Passive Shape Locking for Multi-Bend Growing Inflated Beam Robots," **In:** *2023 IEEE International Conference on Soft Robotics (RoboSoft)* (IEEE, 2023) pp. 1–6.

https://doi.org/10.1017/S0263574726103257 Published online by Cambridge University Press

[84] M. M. Coad, R. P. Thomasson, L. H. Blumenschein, N. S. Usevitch, E. W. Hawkes and A. M. Okamura, "Retraction of soft growing robots without buckling," *IEEE Robot. Autom. Lett.* **5**(2), 2115–2122 (2020).
[85] C. R. Nesler, T. A. Swift and E. J. Rouse, "Initial design and experimental evaluation of a pneumatic interference actuator," *Soft Robot.* **5**(2), 138–148 (2018).
[86] Inc Figaro. Figaro product information, 2022. https://www.figarosensor.com/product/docs/tgs2600_productinformation, Accessed: (14 October 2024).
[87] E. Sariyildiz and K. Ohnishi, "Stability and Robustness Analysis of the Position Control Systems with Disturbance Observer," **In:** *International Conference on Mechatronics and Automation* (IEEE, 2013) pp. 633–638.
[88] P. Müller, K. Salminen, V. Nieminen, A. Kontunen, M. Karjalainen, P. Isokoski, J. Rantala, M. Savia, J. Väliaho, P. Kallio, J. Lekkala and V. Surakka, "Scent classification by k nearest neighbors using ion-mobility spectrometry measurements," *Expert Syst. Appl.* **115**, 593–606 (2019).
[89] E. Vigneau, P. Courcoux, R. Symoneaux, L. Guérin and A. Villière, "Random forests: A machine learning methodology to highlight the volatile organic compounds involved in olfactory perception," *Food Qual. Prefer.* **68**, 135–145 (2018).
[90] P. Tyagi, A. Sharma, R. Semwal, U. S. Tiwary and P. K. Varadwaj, "XGBoost odor prediction model: finding the structure-odor relationship of odorant molecules using the extreme gradient boosting algorithm," *J. Biomol. Struct. Dyn.* **42**(20), 1–12 (2023).
[91] M. Hassan and A. Bermak, "Gas Classification Using Binary Decision Tree Classifier," **In:** *International Symposium on Circuits and Systems (ISCAS)* (IEEE, 2014) pp. 2579–2582.
[92] F. Ba, P. Peng, Y. Zhang and Y. Zhao, "Classification and identification of contaminants in recyclable containers based on a recursive feature elimination-light gradient boosting machine algorithm using an electronic nose," *Micromachines-BASEL* **14**(11), 2047 (2023).
[93] L. R. Bachtiar, C. P. Unsworth, R. D. Newcomb and E. J. Crampin, "Multilayer perceptron classification of unknown volatile chemicals from the firing rates of insect olfactory sensory neurons and its application to biosensor design," *Neural Comput.* **25**(1), 259–287 (2013).
[94] N. L. Husni, A. S. Handayani, S. Nurmaini and I. Yani, "Odor Classification Using Support Vector Machine," **In:** *International Conference on Electrical Engineering and Computer Science* (IEEE, 2017) pp. 71–76.
[95] D. R. Prehanto, I. K. D. N. Aries Dwi Indriyanti and G. S. Permadi, "Classification Based on k-Nearest Neighbor and Logistic Regression Method of Coffee Using Electronic Nose," **In:** *IOP Conference Series: Materials Science and Engineering*, vol. **1098** (IOP Publishing, 2021) pp. 032080.
[96] T. Itoh, Y. Koyama, Y. Sakumura, T. Akamatsu, A. Tsuruta, Y. Masuda and W. Shin, "Discrimination of volatile organic compounds using a sensor array via a rapid method based on linear discriminant analysis," *Sens. Actuators B: Chem.* **387**, 133803 (2023).
[97] D. B. Hibbert, "Bayesian approaches to assigning the source of an odour detected by an electronic nose," *Aust. J. Chem.* **77**(10), p. CH24053 (2024).
[98] I. M. Sari, D. R. Wijaya, W. Hidayat and R. Kannan, "An Approach to Classify Rice Quality Using Electronic Nose Dataset-Based Naïve Bayes Classifier," **In:** *International Symposium on Electronics and Smart Devices (ISESD)* (IEEE, 2021) pp. 1–5.
[99] J. Zaccheus, V. Atogwe, A. Oyejide and A. O. Salau, "Towards successful aging classification using machine learning algorithms," *F1000Research* **12**, 1201 (2024).
[100] P. Berthet-Rayne, S. M. H. Sadati, G. Petrou, N. Patel, S. Giannarou, D. R. Leff and C. Bergeles, "MAMMOBOT: A miniature steerable soft growing robot for early breast cancer detection," *IEEE Robot. Autom. Lett.* **6**(3), 5056–5063 (2021).
[101] R. N. Pietraru, M. Nicolae, Ş. Mocanu and D.-M. Merezeanu, "Easy-to-use MOX-based VOC sensors for efficient indoor air quality monitoring," *Sensors* **24**(8), 2501 (2024).
[102] S. Neubert, T. Roddelkopf, M. F. R. Al-Okby, S. Junginger and K. Thurow, "Flexible IoT gas sensor node for automated life science environments using stationary and mobile robots," *Sensors* **21**(21), 7347 (2021).
[103] S. Botticini, E. Comini, S. Dello Iacono, A. Flammini, L. Gaioni, A. Galliani, L. Ghislotti, P. Lazzaroni, V. Re, E. Sisinni, M. Verzeroli and D. Zappa, "Index air quality monitoring for light and active mobility," *Sensors* **24**(10), 3170 (2024).
[104] Y. Liu, S. Jia, C. K. Yiu, W. Park, Z. Chen, J. Nan, X. Huang, H. Chen, W. Li, Y. Gao, W. Song, T. Yokota, T. Someya, Z. Zhao, Y. Li and X. Yu, "Intelligent wearable olfactory interface for latency-free mixed reality and fast olfactory enhancement," *Nat. Commun.* **15**(1), 4474 (2024).
[105] L. Behnke, B. H. Do, S. Eristoff and R. Kramer-Bottiglio, "Interaction Behaviors of a Vine Robot in a Pipe T-Junction," **In:** *2024 IEEE 7th International Conference on Soft Robotics (RoboSoft)* (IEEE, 2024) pp. 498–503.
[106] C. McFarland and M. M. Coad, "Collapse of Straight Soft Growing Inflated Beam Robots Under their Own Weight," **In:** *International Conference on Soft Robotics (RoboSoft)* (IEEE, 2023) pp. 1–8.

Cite this article: A. J. Oyejide, A. Astar, G. Kaya, U. A. Yaqub, E. A. Baran and F. Stroppa (2026). "A soft growing robotic system for odor detection and classification", Robotica **44**, 630–658. https://doi.org/10.1017/S0263574726103257

https://doi.org/10.1017/S0263574726103257 Published online by Cambridge University Press